Quantifying Reuniens–Hippocampus Tract Integrity in Early Alzheimer's: A Multimodal Voxel-Based Diffusion MRI Approach

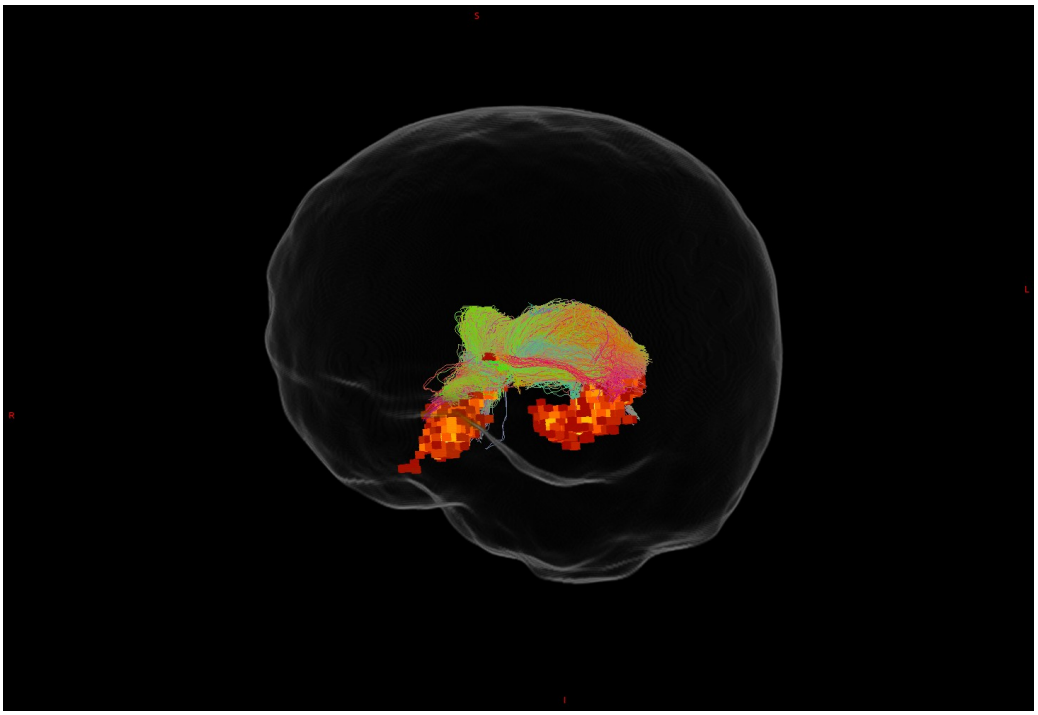

Merel Jager

S3587479

MSc Behavioural and Cognitive Neuroscience: Cognitive track, University of Groningen

Department of Psychology, University of Auckland

Prof. I. Kirk & prof. dr. M. M. Lorist

Abstract

Early detection of disease related changes is crucial for understanding the progression of Alzheimer's disease (AD). The nucleus reuniens (Re) of the thalamus is a key hub in the memory network, yet its structural connectivity remains understudied in human ageing and AD. This study investigated the integrity of the reuniens-hippocampal white matter tract in individuals with amnestic mild cognitive impairment (aMCI) compared to healthy controls, using advanced diffusion MRI tractography and DTI and NODDI modeling techniques. We successfully reconstructed the reuniens-hippocampal tract in all participants and extracted microstructural metrics using both standard voxel-based sampling and a biologically informed SIFT2-weighted approach. While standard analysis showed elevated fractional anisotropy (FA) in aMCI, SIFT2-weighted metrics revealed increased free water fraction (FWF) and orientation dispersion index (ODI), as well as reduced fibre density—a pattern consistent with neuroinflammation and axonal disorganisation. Volume reductions in the Re and hippocampus, along with ventricular enlargement, further supported ongoing neurodegenerative processes. These findings highlight the use of biologically weighted tractography methodology for detecting subtle structural changes and suggest that the reuniens-hippocampal tract may serve as a promising target for early biomarkers of Alzheimer's disease.

Inhoudsopgave

List of abbreviations

Abbreviation	Full Term
ACT	Anatomically Constrained Tractography
AD	Alzheimer’s Disease
aMCI	Amnestic Mild Cognitive Impairment
AxD	Axial Diffusivity
ADC	Apparent Diffusion Coefficient
CSD	Constrained Spherical Deconvolution
CSF	Cerebrospinal Fluid
DTI	Diffusion Tensor Imaging
DWI	Diffusion Weighted Imaging
ECM	Extracellular Matrix
FA	Fractional Anisotropy
FOD	Fibre Orientation Distribution
FSL	FMRIB Software Library
FWF	Free Water Fraction
FW-DTI	Free Water–corrected DTI
iFOD2	Second-order Integration over fibre Orientation Distributions
GM	Gray Matter
MD	Mean Diffusivity
MRI	Magnetic Resonance Imaging
NDI	Neurite Density Index
NODDI	Neurite Orientation Dispersion and Density Imaging
ODI	Orientation Dispersion Index
Re	Nucleus Reuniens
RD	Radial Diffusivity
ROI	Region of Interest
SIFT2	Spherical-deconvolution Informed Filtering of Tractograms 2
TOI	Tract of Interest
WM	White Matter

1 Background

1.1 Introduction

Alzheimer's disease (AD) is the most common age-related neurodegenerative disorder, primarily affecting learning and memory (Alzheimer et al., 1995; Braak & Braak, 1991c). It is clinically characterised by progressive cognitive decline and gray matter pathology. In addition, AD has been associated with disruptions in structural and functional connectivity across brain networks (Bokde et al., 2009; Lo et al., 2010). These alterations often precede the onset of clinical symptoms, making early detection challenging.

AD can be studied across multiple levels of neural organisation: at the cellular level, where pathology includes β-amyloid plaques and tau-related neurofibrillary tangles (Braak & Braak, 1991c; Hardy & Selkoe, 2002). At the regional level, where areas such as the hippocampus and entorhinal cortex show early atrophy (Jack et al., 1997; Braak & Braak, 1991b). And at the network level, in which the disease disrupts connectivity within and between memory-related circuits (Lo et al., 2010).

Diffusion MRI is a non-invasive tool to investigate AD across these levels. It enables inferences about both the microstructural integrity of white matter and the network-level structural connectivity (discussed further in Section 1.4).

Given that such structural changes often emerge before noticeable cognitive symptoms, diffusion MRI is well-suited for studying early stages of Alzheimer's disease, such as amnestic mild cognitive impairment (aMCI). Mild cognitive impairment (MCI) is a heterogeneous condition that lies on a spectrum between normal cognitive ageing and AD. One subtype, aMCI, specifically affects memory and is widely regarded as a prodromal stage of AD (Gauthier et al., 2006; R. C. Petersen et al., 1999). Individuals with aMCI convert to AD at a much higher rate (5–15% annually) than cognitively healthy older individuals (Mitchell & Shiri-Feshki, 2009). Because of this elevated risk, aMCI is often used as a target population for studying early biomarkers and neurodegenerative mechanisms (R. Petersen, 2007).

1.2 Nucleus reuniens

At the regional level of neural organisation, the nucleus reuniens (Re) stands out as a thalamic structure affected early in Alzheimer's disease. Although the thalamus was traditionally viewed as only mildly affected in Alzheimer's disease, Braak & Braak (1991a) identified the Re as one of the few thalamic nuclei with notable neurofibrillary tangle accumulation in post-mortem AD brains.

Recently, a longitudinal study ('Back to Braak') by Censi et al. (2024) extended this observation *in vivo* by comparing stable MCI (sMCI) and converting (cMCI) patients. They found the strongest

volumetric reductions in the Re among 26 thalamic sub-nuclei in the cMCI group, suggesting it may be a sensitive early marker of AD progression.

The Re has been extensively studied in rats, particularly by Robert Vertes and colleagues (Hoover & Vertes, 2012; Varela et al., 2014; Vertes et al., 2007). These studies have shown that the Re is reciprocally connected to the medial prefrontal cortex (mPFC) and several hippocampal subregions, including CA1, subiculum, presubiculum, parasubiculum, entorhinal cortex, and perirhinal cortex. Both the mPFC and hippocampus are critical for spatial working memory, episodic memory, and navigation — cognitive functions known to decline in the early stages of Alzheimer's disease (Vertes et al., 2022).

In humans, however, the Re is a small structure that is difficult to distinguish from neighbouring thalamic nuclei *in vivo*. Although it is not a newly discovered structure, its limited visibility has hindered research. With the development of a probabilistic atlas it has become possible to automatically identify the Re in human imaging data (Iglesias et al., 2018).

1.3 Nucleus reuniens within the Papez circuit

At the network level, the nucleus reuniens is a key node in the limbic system and forms part of the Papez circuit—one of the brain's core memory pathways involved in consolidating episodic memories. This circuit comprises the hippocampus, mammillary bodies, anterior thalamic nuclei, and cingulate cortex, forming a loop that supports hippocampal-cortical communication (Bubb et al., 2017; Papez, 1937).

In Alzheimer's disease (AD), disruptions within the Papez Circuit are associated with anterograde amnesia, reflecting difficulties in forming new memories (Hescham et al., 2020). Hypometabolism of several Papez Circuit regions has also been reported in AD (Villain et al., 2008). Since the Re also shows early signs of damage in AD, like tangles and shrinkage, it may play an important role in how the disease affects this memory network.

Beyond the Papez Circuit, white matter degeneration is now recognised as a hallmark of early AD, potentially preceding or occurring independently of gray matter atrophy (Agosta et al., 2011; Amlien & Fjell, 2014; Fletcher et al., 2013). Tract-based analyses have identified early signs of demyelination and axonal damage in AD (Li et al., 2020), and connectome-level studies suggest that changes in structural connectivity may serve as early biomarkers of disease progression (J. Wang et al., 2012).

As AD disrupts memory networks early on, the connections of the Re, linking the hippocampus and prefrontal cortex, might offer valuable insights into how the disease progresses.

1.4 Diffusion MRI

Currently, the only non-invasive technique to study white matter pathways connecting brain regions *in vivo* is Diffusion Magnetic Resonance Imaging (dMRI). This method relies on the fact that water diffusion in brain tissue is directionally restricted by structures like myelin, axonal membranes, and cell boundaries, making diffusion anisotropic. For example, in healthy white matter, water moves more easily along axons than across them, whereas in cerebrospinal fluid, diffusion is isotropic and unrestricted.

DMRI measures signal attenuation caused by water displacement under magnetic field gradients. This reflects the direction and extent of diffusion, allowing inference of microstructural features like axon density and myelination, that restrict that diffusion. However, since the link is indirect, such interpretations must be made with caution (Jones, 2008).

To address this ambiguity, best practice is to report multiple diffusion measures that capture different aspects of anisotropic behaviour (Gilligan et al., 2019). Various toolboxes and biophysical models have been developed to improve the interpretability of dMRI, and this study applies two models chosen to match the resolution and quality of the acquired data.

1.5 Diffusion models

We use two complementary diffusion models to translate the raw diffusion signal into biologically relevant measures. A classical model called DTI (Basser et al., 1994), that provides general estimates of a sphere that represents directional water diffusion, including fractional anisotropy (FA) and mean diffusivity (MD), axial diffusivity (AxD) and radial diffusivity (RD). These metrics are sensitive to microstructural alterations but non-specific about their underlying cause. A more recent model called NODDI (Zhang et al., 2012) separates the diffusion signal into intra-neurite, extra-neurite, and free water compartments, allowing for more biologically interpretable metrics such as neurite density (NDI), fibre orientation dispersion (ODI) and free water fraction (FWF). Together, these models offer a multidimensional view of white matter structure.

In this study, we use both DTI and NODDI to assess the structural integrity of the Reuniens–hippocampal tract and detect early microstructural alterations in aMCI (see section 2.9). Our approach is guided by previous findings showing that aMCI and early Alzheimer's disease are typically associated with reduced FA and NDI, and elevated MD, RD, ODI, and FWF—patterns indicative of axonal loss, demyelination, and increased extracellular water content (Racin et al., 2014; Zhong et al., 2023). These prior results provide a basis for our hypotheses regarding white matter degeneration in this critical memory pathway.

1.6 Tractography

To isolate the white matter tracts connecting the nucleus reuniens to hippocampal subregions, we use multi-shell, multi-tissue constrained spherical deconvolution (MSMT-CSD) to estimate the directions in which bundles of nerve fibres run within each voxel. This step is crucial because in many brain areas, fibres cross or fan out in different directions, and accurately modelling these patterns helps prevent incorrect reconstruction of tracts (MSMT; Jeurissen et al., 2014; CSD; Tournier et al., 2004).

Using this fibre orientation information, we generate streamlines in MRTrix3.0 (Tournier et al., 2019). Streamlines are virtual paths that approximate the likely routes of white matter pathways. We apply anatomically constrained tractography to ensure these streamlines start and end in biologically plausible regions, based on individual brain anatomy (ACT; R. E. Smith et al., 2012). Specifically, we create subject-specific masks of the Re and hippocampal subregions (CA1, subiculum, entorhinal, and perirhinal cortex) using high-resolution anatomical scans and probabilistic atlases (Iglesias et al., 2015, 2018). These masks define the start and end points of each streamline, helping us trace the pathway that links these memory-related regions.

To quantify microstructural properties along these tracts, we use two complementary voxel-based approaches. First, we apply a conventional method that samples diffusion metrics from all voxels intersected by the streamlines, assuming equal contribution (F. Zhang et al., 2021). This may not hold in regions with poor reconstruction or anatomical variability. To address this, we apply a second SIFT2-weighted approach, which assigns biologically informed weights to each streamline based on its agreement with the underlying fibre orientation distributions (R. E. Smith, Tourner, et al., 2015). This weighting reduces the influence of implausible or noisy streamlines and emphasises anatomically plausible trajectories. Using both methods allows us to compare conventional voxel-based estimates with a biologically weighted alternative and assess whether SIFT2 improves sensitivity to early microstructural changes in aMCI.

In addition to microstructural metrics, we compute a connectivity strength measure; the total SIFT2-weighted fibre density of the tract. This quantifies the overall strength of the Re–hippocampus tract and enables comparison between aMCI and control participants (F. Zhang et al., 2021).

Together, these tract-specific methods allow us to examine a subcortical pathway that may show early microstructural alterations in Alzheimer's disease.

1.7 Aim and hypothesis

This study investigates whether our methodology can capture the (micro)structural integrity of the reuniens–hippocampal white matter pathway, and whether this tract shows alterations in individuals with amnestic mild cognitive impairment (aMCI) compared to healthy controls.

We quantify diffusion-based metrics (DTI: FA, MD, RD, AxD; NODDI: NDI, ODI, FWF) and mean fibre density within this tract to assess whether these measures reflect early neurodegenerative processes.

We hypothesise that the structural integrity of the reuniens–hippocampal white matter tract is reduced in individuals with aMCI compared to healthy controls, reflecting early neurodegenerative processes. Specifically, we expect: 1) Our tractography approach to successfully reconstruct the connection between the nucleus reuniens and hippocampus; 2) Lower FA, AD, and NDI, and higher MD, RD, ODI, and FWF in aMCI, consistent with reduced diffusion restriction due to neurodegeneration; and 3) Lower SIFT2-weighted fibre density in aMCI participants, indicating decreased tract connectivity.

To our knowledge, this is the first *in vivo* human dMRI study to focus on this specific tract. By doing so, we aim to identify early connectivity disruptions in Alzheimer's disease and offer a methodological framework for tracking small but functionally important tracts in future studies.

2. Methods

2.1 Participants

27 healthy controls and 48 aMCI participants were included in this study. Participants with aMCI were recruited either via referral from their general practitioner, medical specialist, or a clinician affiliated with the Auckland District Health Board, who identified concerns regarding the individual's memory and/or cognitive functioning. Additional recruitment occurred through other ongoing studies related to cognitive and memory impairments. Control participants without MCI were recruited via the Research Volunteer Register at the Centre for Brain Research and through community advertisements in Auckland, New Zealand.

AMCI participant inclusion criteria required them to be over the age of 55, fluent in English, and experiencing memory and/or cognitive difficulties. Exclusion criteria included a history of major head trauma, cerebrovascular conditions, neurological disorders (excluding aMCI), substance abuse or dependence, psychiatric illness, or long-term use of psychiatric medications. Control participants were subject to the same criteria, with the added requirement that neither the participant, their relatives, nor healthcare professionals reported any memory or cognitive concerns.

The study received ethical approval from the Auckland District Health Board, and all participants gave written informed consent prior to participation.

2.2 Clinical assessment

Participants underwent an initial clinical session at the Dementia Research Clinic, part of the Clinical Research Centre on the Grafton Campus of the University of Auckland. The session was 90-120 minutes in time and included structured interviews, lifestyle evaluations, and behavioural assessments. Each participant was encouraged to bring an informant; someone familiar with their day-to-day functioning. With consent from both parties, a medical specialist conducted an interview with the informant to collect additional behavioural and clinical information.

To assess neuropsychiatric and functional symptoms, all participants completed standardised questionnaires, including the Neuropsychiatric Inventory Questionnaire (NPI-Q), the Everyday Cognition scale (ECog), and the Functional Activities Questionnaire (FAQ).

After this initial session, each participant was evaluated by a medical specialist together with a neuropsychologist and research nurse. They used cognitive screening outcomes, functional assessments, and medical history to classify individuals as either cognitively normal or as having aMCI.

2.3 MRI acquisition

In a second session, participants underwent magnetic resonance imaging (MRI) at the Centre for Advanced MRI (CAMRI) at the University of Auckland. The total scanning duration was approximately 45 minutes, including 5 minutes for preparation.

Diffusion-weighted imaging (DWI) was performed on a Siemens 3 Tesla MAGNETOM Skyra scanner (Erlangen, Germany) with a 70 cm bore and a 32-channel head coil. The diffusion sequence used an echo-planar imaging protocol with the following parameters: TR = 3680 ms, TE = 101.6 ms, flip angle = 78°, and slice thickness = 2 mm. Data were acquired at three diffusion weightings: b = 0 s/mm² (5 volumes), b = 1000 s/mm² (50 volumes), and b = 2000 s/mm² (50 volumes). The DWI sequence lasted approximately 6.37 minutes.

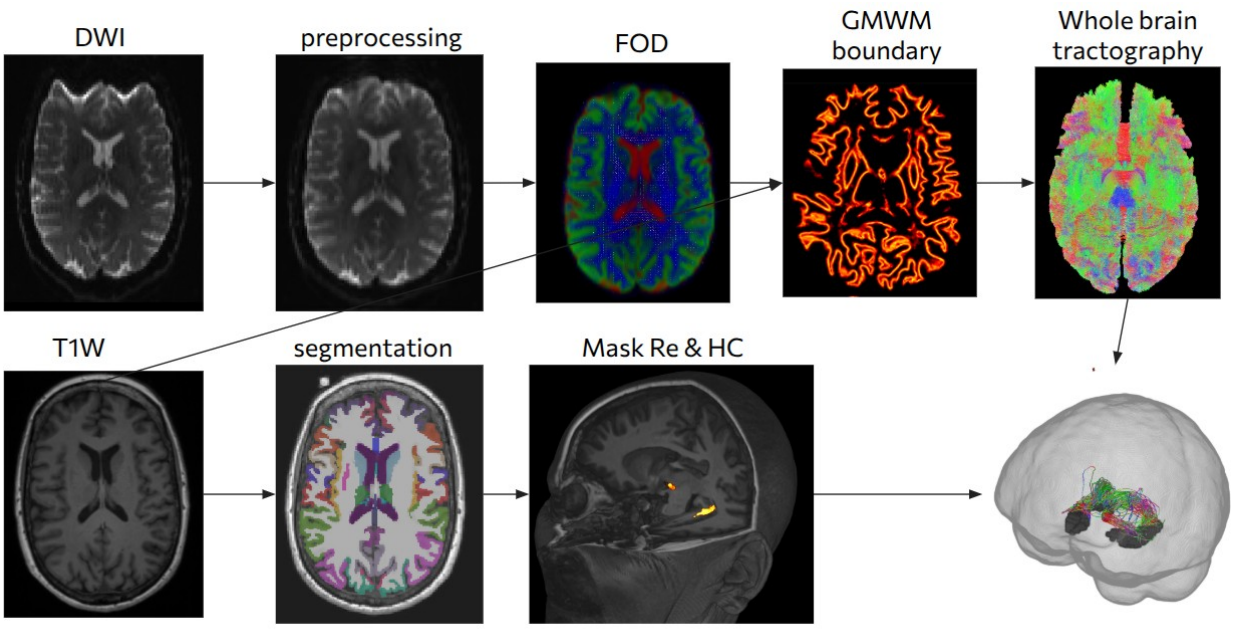

Figure 1: Schematic flowchart of tract of interest filtering using tractography of diffusion weighted imaging and parcellation of T1-weighted images. DWI = diffusion weighted imaging, T1W = T1 weighted images, FOD = Fibre orientation distribution, GMWM = Grey Matter White Matter, Re = Nucleus Reuniens, HC = Hippocampus.

2.4 MRI data preprocessing

An overview of the data processing pipeline is presented in Figure 1.

All diffusion data was preprocessed with Mrtrix3 (Tournier et al., 2019), FMRIB Software Library (FSL) (Jenkinson et al., 2012), Freesurfer (Fischl, 2012) and ANTS (Tustison et al., 2021). Quality checks were performed in between steps by visually inspecting the derived scans. The following steps were preformed to preprocess the data: converting to *.mif* format using *mrconvert*, denoising using *dwidenoise* (Veraart et al., 2016), removing gibbs-ringing artefacts using *mrdegibbs* (Kellner et al., 2016). Then b0-field inhomogeneity correction using *topup,* FSL (Andersson et al., 2003; S. M. Smith et al., 2004a), brain mask estimation using *BET,* FSL (S. M. Smith, 2002) and eddy- current and movement distortion correction using *eddy,* FSL (Andersson & Sotiropoulos, 2016). B1 bias field was corrected twice based on the mean b=0 image using the N4 algorithm to improve brain mask estimation using *dwi2mask* (Tustison et al., 2010).

2.5 Fibre orientation distribution

Multi-shell multi-tissue constrained constrained spherical deconvolution (MSMT; (CSD; is performed as follows: response functions were estimated using *dwi2response* and the *dhollander* algorithm (Dhollander et al., 2016). Using the response functions for 3 tissue types, per voxel the orientation of all fibres crossing that voxel is estimated, resulting in the fibre orientation distribution (FOD) with *dwi2fod msmt_csd* (Jeurissen et al., 2014; Tournier et al., 2004, 2007). Last, the data is

corrected for global intensity differences using *mtnormalise* (Dhollander et al., 2021; Raffelt et al., 2017).

2.6 Whole brain tractography

Anatomically constrained tractography (ACT; R. E. Smith et al., 2012) was performed, using the T1-weighted image for segmentation into 5 different tissue types (5tt) (cortical and subcortical gray matter (GM), white matter (WM), cerebral spinal fluid (CSF) and pathological tissue) using *5ttgen fsl -sgm_amyg_hipp* (Patanaude et al., 2011; S. M. Smith, 2002; S. M. Smith et al., 2004b; Y. Zhang et al., 2001). To create the transformation matrix, the GM (volume 0) was extracted from the 5tt using *fslroi.* The meab b0 of diffusion space was co-registered to this volume 0 using *flirt -interp nearestneighbour -dof 6.* The matrix output was then converted to MRtrix format using *transformconvert flirtimport*. To define where the streamlines should not end, such as the CSF, and where they should start, such as the gray matter white matter (GM/WM) boundary, a mask of the GM/WM boundary was created using *5tt2gmwmi.* Thereafter, probabilistic fibre tractography was performed using *tckgen -act -backtrack -seed_gmwm -minlength 5 -maxlength 250 – cutoff 0.06 -angle 45 -select 10000000.* This command used ACT and the second order integration over fibre orientation distributions (iFOD2) algorithm (Tournier et al., 2010), which enables the tracking of curved and crossing fibres by integrating over uncertainty at each step, rather than always choosing the dominant direction, see Figure 2. 10 million streamlines per participant were selected, based on the normalised fibre orientations of WM. Finally, SIFT2 was applied to assign a weight to each streamline based on how well it fits the underlying FODs. These weights, estimated using *tcksift2 -act -fd_thresh 0.02* (R. E. Smith, Tourner, et al., 2015), are proportional to the local fibre density derived from spherical deconvolution, allowing for a more biologically accurate quantification of white matter connectivity.

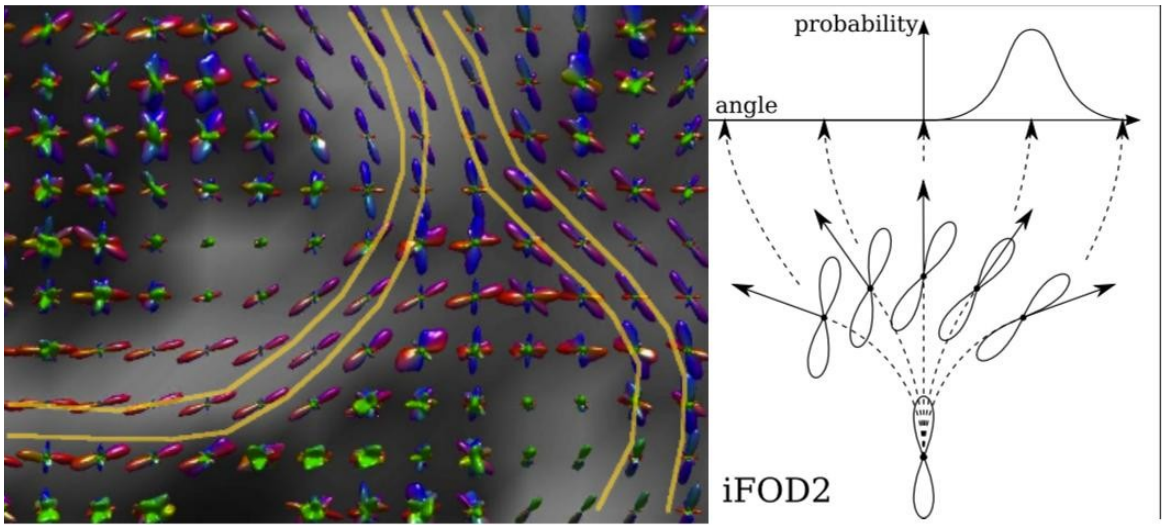

Figure 2: Schematic figure of probabilistic fibre tracking using fibre orientation distribution estimates per voxel. Left: Example (Daducci et al., 2012) of fibre orientation distributions (FODs) visualised as coloured lobe shapes, representing multiple fibre populations within each voxel. The yellow lines show possible streamlines generated . Right: schematic (from Tournier et al., 2010) of probabilistic sampling strategy in iFOD2 algorithm, integrating over uncertainty at each step, rather than always choosing the dominant direction.

2.7 Segmentation & mask creation

Structural T1-weighted images were processed using the *recon-all* pipeline from FreeSurfer v7.3.2 including brain extraction and skull stripping (Segonne et al., 2004), estimating Total Intracranial Volume (eTIV) – later used in analysis - (Buckner et al., 2004), subcortical segmentation (Fischl et al., 2002), perirhinal labelling (Augustinack et al., 2013) and the rest of automated anatomical labelling, was based on the Desikan-Killiany atlas (Desikan et al., 2006). The perirhinal and entorhinal labels were converted to volumes using *mri_label2vol.*

For thalamic nuclei segmentation the atlas by (Iglesias et al., 2018) was used, and for hippocampal subfield segmentation the atlas by (Iglesias et al., 2015). Voxels labelled 8116 and 8216 were extracted for the left and right Re, respectively, using *mrcalc.* Hippocampal masks included regions labeled 203 (parasubiculum), 233 (presubiculum-head), 234 (presubiculum-body), 235 (subiculum-head), 236 (subiculum-body) and 238 (CA1-body). Segmentations were visually inspected to ensure the extracted regions approximately corresponded to the expected locations. The voxel counts of these segmentations were used in later analysis. These hippocampal subfields were merged to form a composite 'expanded CA1' mask, using *mrcalc,* reflecting the Re's known connectivity targets in rodent studies (Section 1.2). Because of the upcoming conversion to DWI space, which has a lower resolution, a small area or surface like the Re/CA1 can easily get lost. To ensure that these voxels did not vanish, the outsides of the Re and expanded CA1 part were dilated by 2 voxels in T1 space, using *maskfilter -npass 2.* Then, the masks were regridded to T1 space to make sure they all share the same coordinates, using *mrgrid -interp nearest.* The expanded CA1, entorhinal and perirhinal masks were merged into a hippocampal part and was binarised at 0.3 and all voxels were assigned the value of 2. The Re part was too binarised at 0.3 and these voxels got the value of 1. These two again were merged into one complete mask per hemisphere, that was transformed to dwi space using *mrtransform -linear "transformation matrix" -inverse -template "dwi_image" -interp nearest.* The outputs of this masking pipeline is henceforth called regions of interest (ROIs).

2.8 Tract of interest

Using *tck2connectome -symmetric* the ROIs were assigned to 2 nodes in the parcellation scheme, according to the voxel values: the Re part to node 1 and hippocampal part to node 2. By using the reverse *connectome2tck -nodes 1,2 -exclusive -files single*, streamlines are selected that terminate within a 2mm radius of the node, a technique called 'local search' (R. E. Smith, Tournier, et al., 2015). This is a more inclusive approach that makes the exact edges of the masks less influential for selection of streamlines. Then, streamlines were filtered based on a maximum length threshold: max = mean length +1.6 * SD (standard deviation). All along, weights corresponding with the streamlines were selected. Using *tckmap -contrast tdi* (Calamante et al., 2010), a mask was created covering the

selected streamlines, henceforth referred to as the tract of interest (TOI). Last, that mask was then binarised returning every non-zero voxel as a value of 1, to make sure every voxel is included.

2.9 Metrics

To quantify the microstructural properties of the TOI, we computed voxel wise parametric maps from DTI and NODDI models. All maps were registered to the subject-native diffusion space, and values for each metric were sampled within the TOI mask for each subject and hemisphere.

DTI models diffusion as a single tensor (spherical 3D vector) per voxel. DTI metrics were computed using *dwi2tensor* and *tensor2metric* in MRtrix (see Figure 3): Fractional anisotropy (FA): reflects the degree of directional preference of water diffusion. Mean diffusivity (MD): captures the average diffusivity in all directions. Axial diffusivity (AxD): reflects diffusivity along the principal axis of the tensor. And radial diffusivity (RD): reflects diffusivity perpendicular to the principal axis.

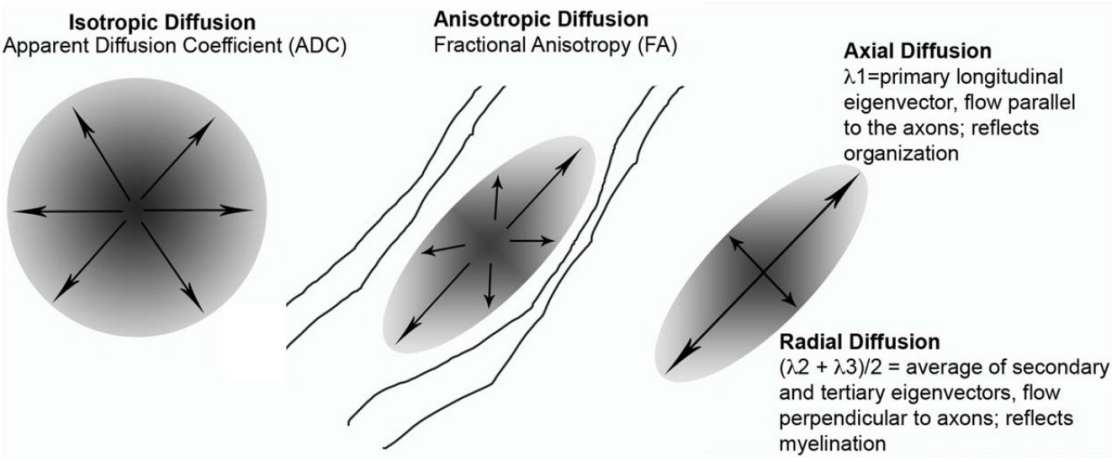

Figure 3: Diffusion tensor imaging (DTI) metrics.
Illustration of isotropic (ADC/MD) and anisotropic diffusion. Axial diffusivity (AD) reflects diffusion along fibres; radial diffusivity (RD) reflects diffusion perpendicular to fibres; fractional anisotropy (FA) captures overall directionality. Adapted under CC BY-ND 4.0 license.

NODDI distinguishes the contribution of 3 compartments to the diffusion signal. NODDI metrics were computed using the AMICO toolbox (version 2.1.0) (Daducci et al., 2015) in MATLAB (see Figure 4): Neurite density index (NDI) (also called FICVF): reflects the volume fraction of axons and dendrites (intra-neurite space). The orientation dispersion index (ODI): quantifies the variability in neurite orientation, enabling differentiation between coherent and dispersed fibre configurations. And the free water fraction (FWF) (also called FISO): Estimates the fraction of isotropically diffusing water, such as CSF, in each voxel. This metric enables correction for partial volume contamination, especially relevant near ventricular boundaries.

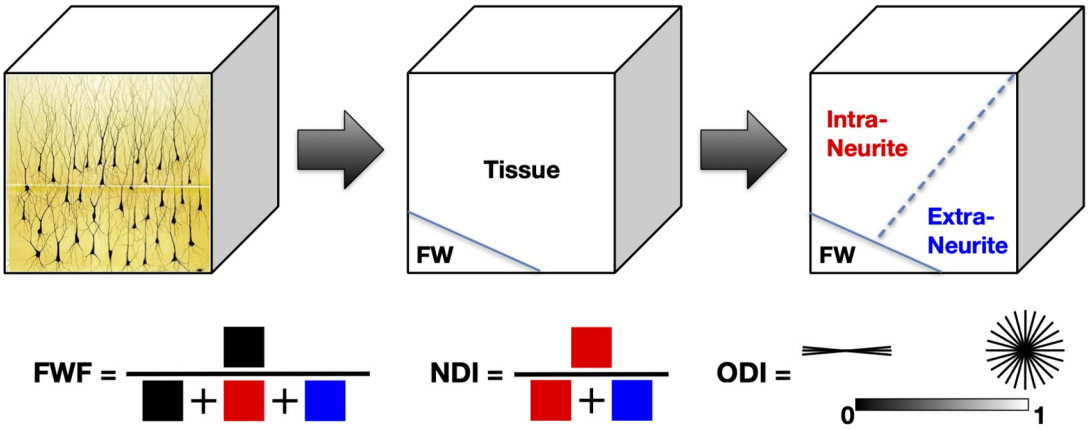

Figure 4: NODDI model components
Shows how the NODDI model separates the diffusion signal into free water (FW), intra-neurite, and extra-neurite compartments. Derived metrics include free water fraction (FWF), neurite density index (NDI), and orientation dispersion index (ODI), which reflects angular variation of neurites.Adapted under CC BY-ND 4.0 license.

2.10 Methods for calculating tract-average

An overview of the data processing pipeline is presented in Figure 5. As mentioned, two methods for calculating the tract-average metric are used:

Method 1: full voxel based

For each subject and hemisphere, the mean diffusion value within the TOI was calculated by averaging the metric values across all voxels included in the mask, using MRtrix's *mrstats*:

$$\text{Mean}_i = \frac{1}{N_i} \sum_{v \in \text{TOI}_i} x_{iv}$$

Where x_{iv} is the diffusion metric value in voxel v of subject i, and N_i is the total number of voxels in the TOI mask for that subject and hemisphere. This unweighted method provides a straightforward voxel-based summary of tract microstructure.

Method 2: weighted mean using SIFT2

To obtain biologically meaningful estimates of tract microstructure, we computed streamline-level weighted means using SIFT2. This method incorporates both voxel-level diffusion values and the anatomical plausibility of each streamline. Importantly, voxels may be sampled multiple times if traversed by multiple streamlines, making this a streamline-based (not purely voxel-based) approach.

For each subject and hemisphere, mean microstructural metrics along the streamlines were extracted using MRtrix's *tcksample*. Each value was paired with a SIFT2-derived weight, representing its contribution to cross-sectional fibre density based on the underlying FOD (R. E. Smith, Tourner, et al., 2015). To correct for inter-subject differences in absolute weight magnitudes—typically higher in

healthy controls—we normalised weights by dividing each by the participant's mean SIFT2 weight. This yielded relative within-subject weights, ensuring comparability across participants.

Weighted means of the TOI were computed as:

$$\text{Weighted Mean}_i = \frac{\sum_j w_{ij} \cdot x_{ij}}{\sum_j w_{ij}}$$

where x_{ij} is the diffusion value for streamline j in subject i, and w_{ij} the normalised SIFT2 weight for streamline j in subject i. These streamline-weighted means include more information and were used for group comparisons of microstructural integrity in the reuniens–hippocampus tract.

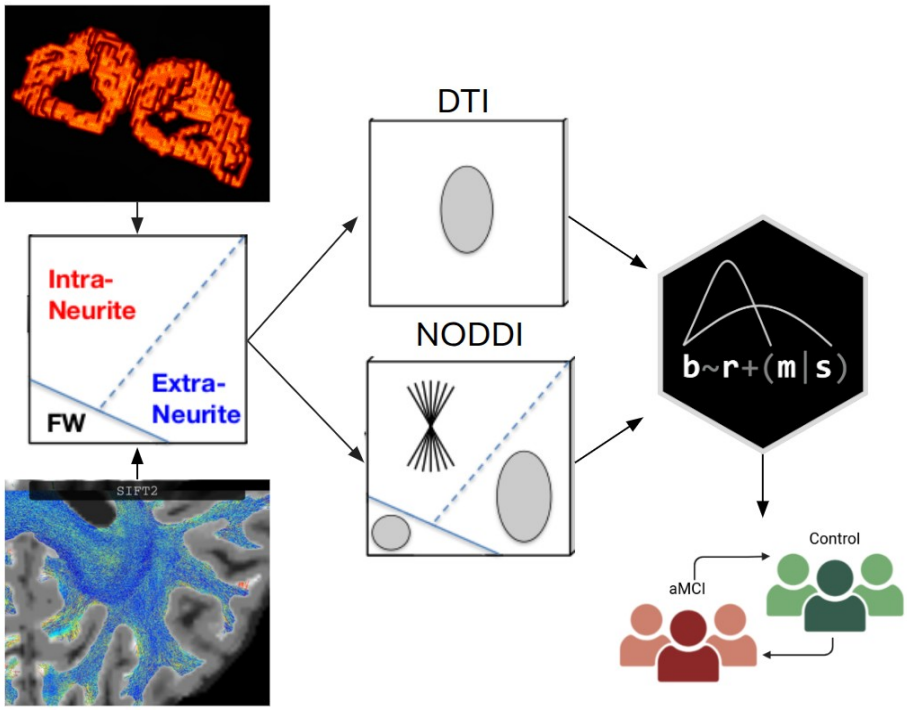

Figure 5: Schematic flowchart of 2 methods and multivariate analysis of the tract of interest. SIFT2 = spherical informed filtering of tactogram 2, FW = Free Water, DTI = Diffusion Tensor Imaging, NODDI = Neurite Orientation Dispersion and Density Imaging, brms = Bayesian regression modeling using Stan, aMCI = amnestic Mild Cognitive Impairment.

2.11 Fibre density

To quantify structural connectivity, we computed SIFT2-weighted fibre density maps and integrated them with voxel-level DTI and NODDI metrics.

Fibre Density Computation

For each subject and hemisphere, streamlines were projected into voxel space using *tckmap* with *-tck_weights_in* and *-precise* options, applying SIFT2-derived weights. This yielded a voxel-wise map of weighted fibre density, approximating apparent fibre density or the total cross-sectional area of fibres per voxel (R. E. Smith, Tourner, et al., 2015). Apparent fibre density values were restricted to TOI binary mask, and mean fibre density per subject and hemisphere was extracted using *mrstats*.

Integration with Diffusion Metrics

To visualise tract-level microstructural profiles, apparent fibre density maps were voxel-wise multiplied with DTI (FA, AD, RD) and NODDI (NDI, ODI, FWF) maps using *mrcalc*, after resampling and converting all inputs to *.mif* format. These fibre density × metric maps were rendered in streamline space to explore local variation across individuals and groups. Importantly, these visualisations were for illustrative purposes only; group-level statistical analyses used separately computed tract-level summary values.

2.12 Statistics

The primary goal of the statistical analysis is to investigate whether the seven diffusion metrics, after accounting for confounding factors such as age, gender, hemisphere, and estimated total intracranial volume (eTIV), contain information about neurodegeneration, an unobserved latent variable. We formalise through a directed acyclic graph (DAG), which depicts assumed causal relations among the observed and unobserved variables involved in the analysis (McElreath, 2020). The DAG of this research is shown in Figure 6.

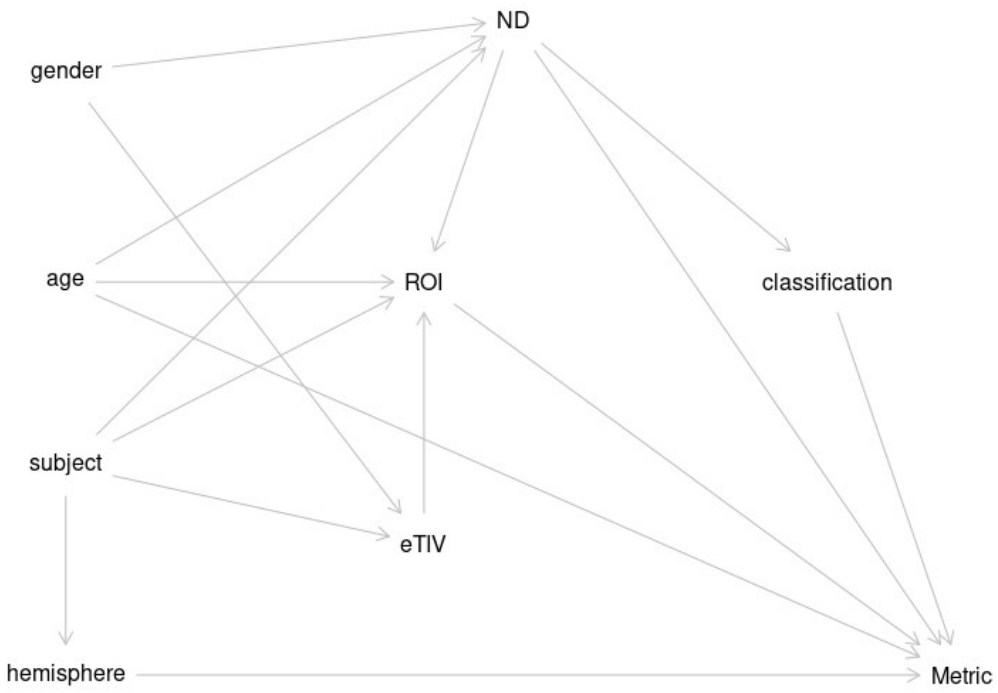

Figure 6: Directed Acyclic Graph (DAG) depicting hypothesized relationships among variables influencing microstructural metrics. ND = Neurodegeneration, ROI = Region Of Interest, eTIV = estimated Total Intracranial Volume.

Basic demographic data is tested on group differences using the Bayesian chi-square test for gender (a dichotomous variable) and Bayesian independent samples t-test for the other continuous variables, performed in JASP (version 0.19.3: https:/jasp-stats.org/) (van Doorn et al., 2021).

Bayes factors (BF_{10}) were used to quantify the strength of evidence for group differences. The BF_{10} expresses how much more likely the data are under the alternative hypothesis (H_1) compared to the null hypothesis (H_0); values above 1 indicate support for H_1, while values below 1 indicate support for H_0. Interpretation followed conventional thresholds (e.g., BF_{10} 1-3 = anecdotal evidence, 3-10 = moderate evidence, 10-30 = strong evidence, 30-100 = very strong evidence, > 100 = extreme evidence (Lee & Wagemakers, 2015)).

All other statistical analyses were performed in Rstudio (version 2024.12.1+563) and therefore used R (version 4.4.2, http://cran.r-project.org/). Bayesian regression models using stan (brms) was used (Burkner, 2017, 2018; Carpenter et al., 2017) to test evidence for group differences in white matter between aMCI and control. Two multivariate hierarchical models were fitted to the data, the first expressed the four DTI metrics (FA, ADC, RD, AD) and the second modelled the three NODDI metrics (FICVF, ODI, FISO), while accounting for hemisphere, age, gender and estimated intracranial volume (eTIV) and adding a random intercept per participant. The metrics, age, ROI size and eTIV were standardised (z-transformed) and used in the model that ran 4 Markov chains Monte Carlo (warmup = 1000, iterations = 4000, seed = 666). The Bayesian multilevel models overcome inefficiencies and over-penalties in current univariate models and corrects for multiple testing (Chen et al., 2019).

Bayesian inference is expressed in terms of the whole posterior distribution of each effect of interest. Instead of standard significance testing, we inferred credibility of evidence from posterior distributions by a positive posterior probability (P+). This is the probability that the posterior is greater than zero. By computing classification contrast posteriors, this generates a P+ to test group differences. Moderate evidence is indicated by a positive posterior probability (P+) of <0.10 or >0.90, strong evidence by a P+ of <0.05 or >0.95, and very strong evidence by a P+ of <0.025 or >0.975 (Chen et al., 2019).

3 Results

Table 1: Demographical and clinical information of the participants

Descriptor	Control N = 27	aMCI N = 48	BF_{10} (aMCI vs Control)	Error %
per participant				
Age (years) ± SD	66.4 ± 9.3	69.0 ± 7.7	0.85	0.02
Gender (female) ± SD	22 (81.5%)	26 (54.2%)	**332.91**	0
ACE Score ± SD	94.96 ± 4.34	87.58 ± 6.64	**5527.91**	5.273×10-6
eTIV (mm3) ± SD	150500.0 ± 13228.8	1481666.7 ± 7637.6	1.19	0.01

Bold indicates moderate or greater evidence. Control = healthy control; aMCI = amnestic mild cognitive impairment; SD = standard deviation; ACE = Addenbrook's Cognitive Examination; eTIV = estimated total intracranial volume, BF_{10} = Bayes factor H1 over H0.

3.1 AMCI and control groups differ in gender and cognitive scores

A total of 27 control and 48 aMCI classified participants were enrolled in the present study. See Table 1 for all demographics. Extreme evidence is found for a difference in ACE scores (BF_{10}=5529.91, 5.273×10-6), which contributed to group assignment, and for gender (BF_{10}=332.91, 0), where the control group comprised 22 females (81.5%), while the aMCI group included 26 females (54.2%). No evidence was found for a difference in age (BF_{10}=0.85, 0.02) or eTIV (BF_{10}=1.19, 0.01) between the groups.

3.2 Reuniens–hippocampal tract successfully reconstructed

Figure 7 shows streamlines that connect the reuniens region with the hippocampal subregions, for both an aMCI and control subject. Most streamlines take a posterior route. However, in some cases (more so in the aMCI group compared to the control group) streamlines take an anterior route, see Figure 7, right panels which shows all subjects warped together. All panels show a combined mask, where voxels shared by more participants have brighter colours.

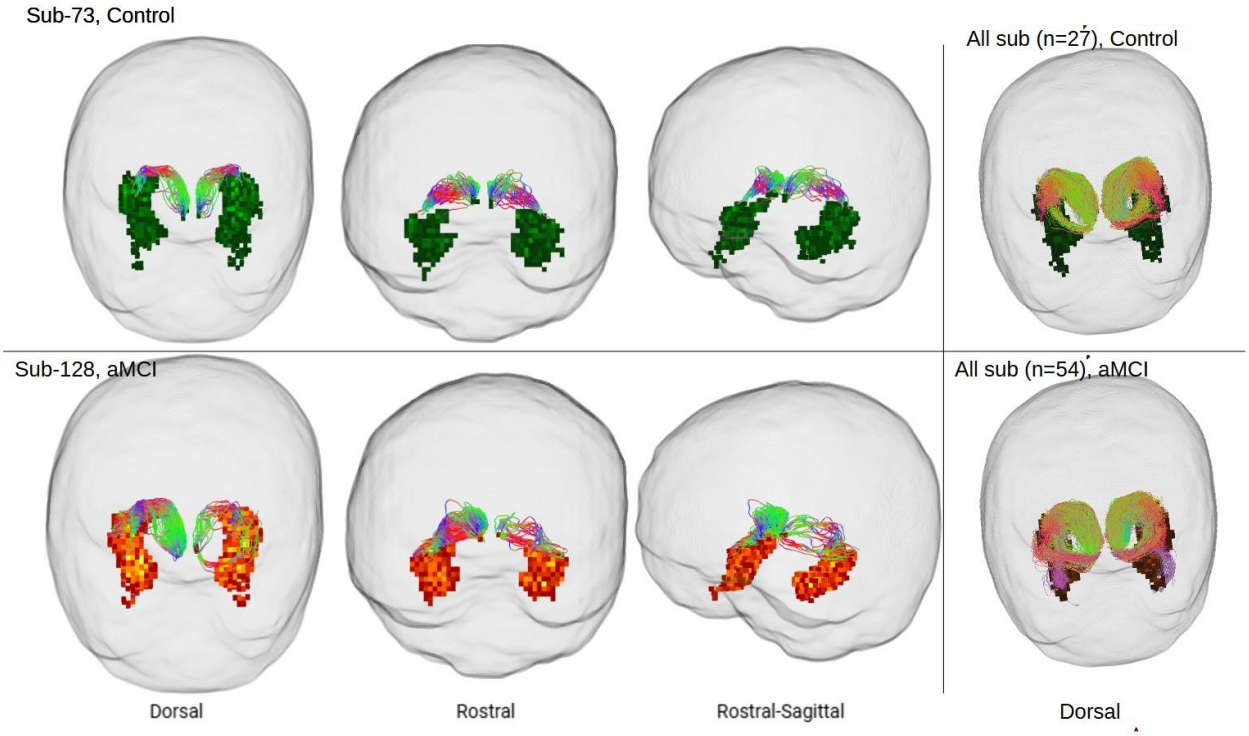

Figure 7: Streamlines connecting reuniens and hippocampal regions. Left 6 panels are single subject, top: subject 73, bottom: subject 128. streamline colour represents direction. green = anterior posterior, red = lateral medial, blue = rostral caudal. green mask = control, orange mask = aMCI, amnestic mild cognitive impaired. colour intensity = shared voxel position of mask. Right two panels: all subjects warped to MNI space, streamlines in low density areas filtered out. Top = control, bottom = aMCI. streamline colours represent endpoints. sub = subject, n = number.

3.3 Smaller Re and hippocampus volumes and enlarged ventricles in aMCI

Table 2: Neuroanatomical descriptives

Descriptor	Control	aMCI	BF_{10} (aMCI vs Control)	Error %
per hemisphere	N = 54	N = 96		
HC mm3 ± SD	2816.7 ± 76.4	2591.7 ± 38.2	**178.71**	1.232×10-8
Re mm3 ± SD	1250.0 ± 50.0	950.0 ± 50.0	**9244.74**	7.686×10-11
N Streamlines ± SD	460.0 ± 10.0	400.0 ± 10.0	2.57	0.01
lat_vent_rel			**10.01**	0
third_vent_rel			**14.2**	2.190×10-7

Bold indicates moderate or greater evidence. aMCI = amnestic Mild Cognitive Impairment, HC = Hippocampus, Re = Reuniens, N = Number, SD = standard deviation, lat_vent_rel = lateral ventricle relative size, third_vent_rel = third ventricle relative size.

Compared to controls, the aMCI group showed fewer voxels in both the hippocampus (*Mean (M)* = 2591.7 vs. 2816.7; BF_{10} = 178.71) and nucleus reuniens (*M* = 950.0 vs. 1250.0; BF_{10} = 9244.74), both with extreme evidence. The number of reconstructed streamlines connecting Re and hippocampus showed anecdotal evidence for being reduced in aMCI (*M* = 400.0 vs. 460.0; BF_{10} = 2.57). Strong evidence was found for lateral ventricle volume relative to intracranial volume being higher in aMCI (BF_{10} = 10.01), and for enlarged third ventricle size (BF_{10} = 14.2). Descriptives are shown in Table 2. Group comparisons for both ventricle volumes are shown in Figure 8 (first and third panel).

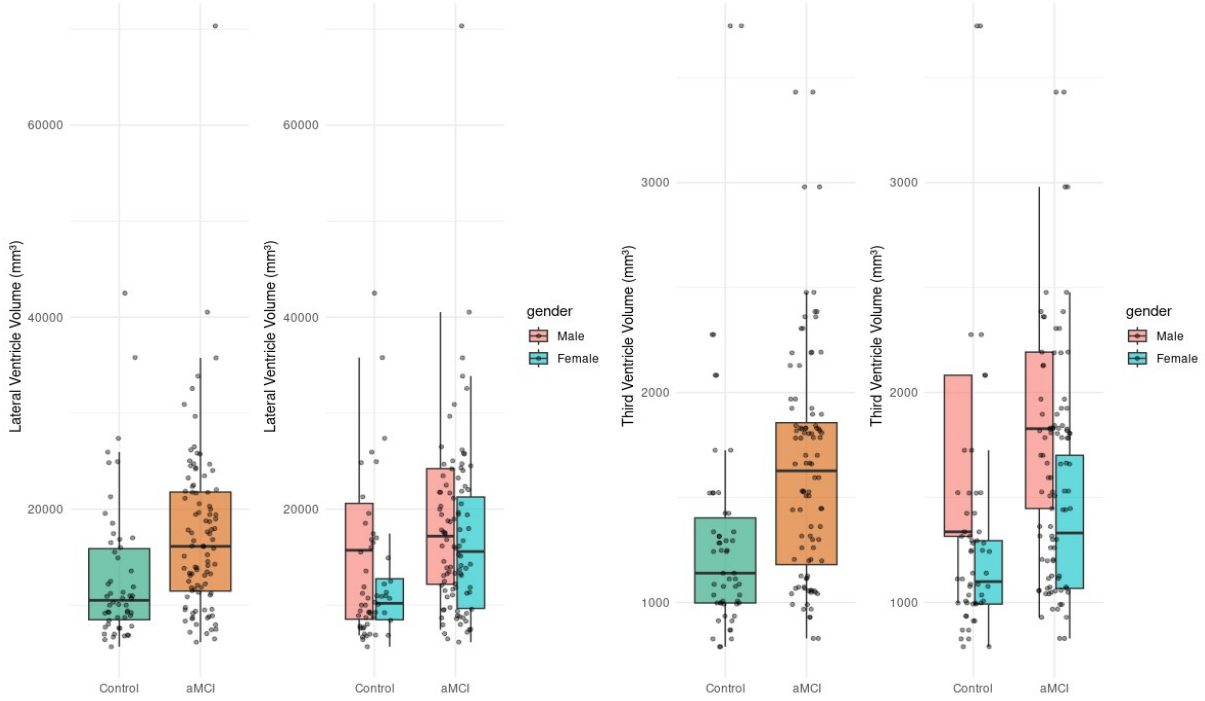

*Figure 8: Lateral and third ventricle volumes by diagnostic group and gender. Boxplots show the distribution of lateral (**left** panels) and third ventricle (**right** panels) volumes across aMCI and control participants, with additional stratification by gender, pink = male, blue = female. AMCI = amnestic mild cognitive impaired. Individual data points are overlaid to illustrate within-group variability. Volumes are reported in mm³.*

Gender-stratified post hoc inspection of third ventricle volume (Figure 8, second and fourth panel, caution; colours are counter-intuitive) suggests that males tended to have larger third ventricles, than females in both groups. Given the unequal gender distribution across groups—particularly the over representation of females in the control group—these volumetric findings should be interpreted with caution. This is further discussed in Section 4.6.

3.4 Unweighted increase in FA, SIFT2-weighted increase in FWF and ODI in aMCI

We assessed classification effects (aMCI vs. control) across both non-weighted and SIFT2-weighted voxel- based diffusion metrics using Bayesian multilevel modelling. Posterior distributions of the effect sizes are visualised in Figure 9, where the y-axis is ordered on effect size.

In the non-weighted model (Figure 9, top), moderate evidence was observed for higher FA in aMCI compared to controls ($P^+ = 0.9375$). Anecdotal evidence is found for ADC ($P^+ = 0.1768$) and ODI ($P^+ = 0.1596$), and RD showed weak-to-moderate evidence for being lower in aMCI compared to control ($P^+ = 0.1054$). All other metrics (NDI, AxD, FWF) showed insufficient evidence for a group difference (all P^+: [0.7147, 0.3609]). In contrast, the SIFT2-weighted model (Figure 9, bottom) revealed moderate evidence for higher FWF ($P^+ = 0.9235$) and ODI ($P^+ = 0.9213$) in aMCI. For weighted NDI, AxD, RD, ADC, and FA, the posterior distributions were centred around zero with no evidence for group differences (P^+: [0.7948, 0.3563]).

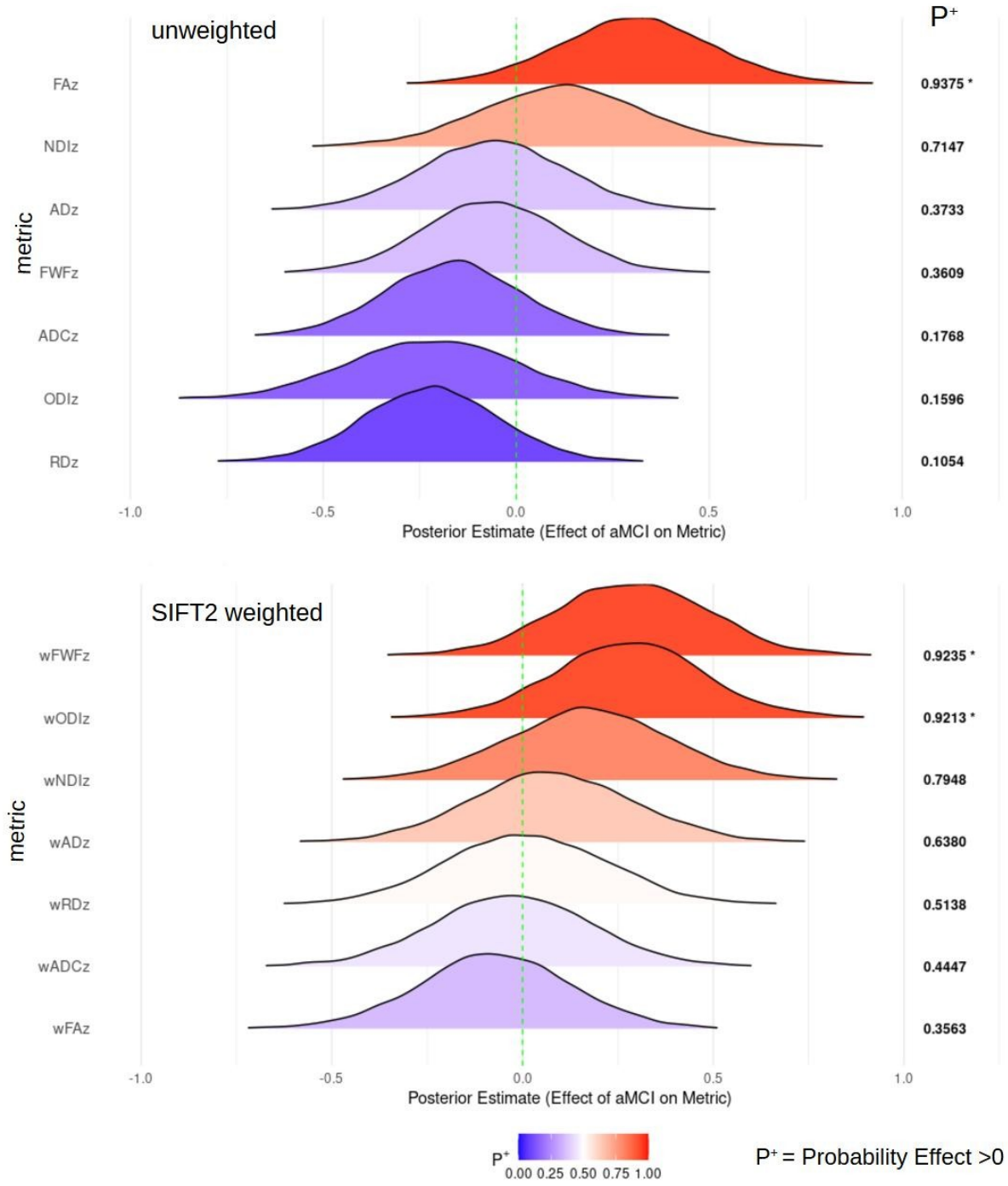

*Figure 9: Posterior Distribuitons of Classification Effect (aMCI vs Control) on Diffusion Metrics. Displaying posterior distributions for the effect of classification of diffusion MRI metrics extracted from the tract. Panel 1 (top): shows unweighted (standard voxel-averaged) approach. Panel 2 (bottom): shows SIFT2-weighted approach. Green midline = no difference, right shift means increased values in aMCI vs controls. P+ = posterior positive probability, w = weighted, z = z-scored, ADC = apparent diffusion coefficient, AD = axial diffusivity, FA = fractional anisotropy, FWF = free water fraction, NDI = neurite density index, ODI = orientation dispersion index, RD = radial diffusivity. Ranked based on effect size. * = moderate evidence.*

3.5 AMCI tracts more anterior and fragmented; SIFT2 enhances anatomical specificity

Tractography of the reuniens-hippocampal tract for a representative sample of 6 subjects from each group as viewed from below, is shown in Figure 10. Most streamlines show a symmetric curvature from the midline thalamic region posteriorly and laterally into the hippocampus on each side. In the control group, this structure is more complete and densely bundled, whereas in many aMCI participants, the arcs appear fragmented, sparser and more streamlines follow anterior routes. Visual inspection of the colouring based on heat maps of the FA (top rows), show that high FA is also rewarded to less plausible fibres, while multiplying FA by SIFT2 weighted fibre density maps (middle rows) highlights more anatomically robust streamlines. When multiplying the fibre density map with the FWF map (bottom rows), streamlines that align ventricles (those on the hind side of the streamlines) show increased FWF.

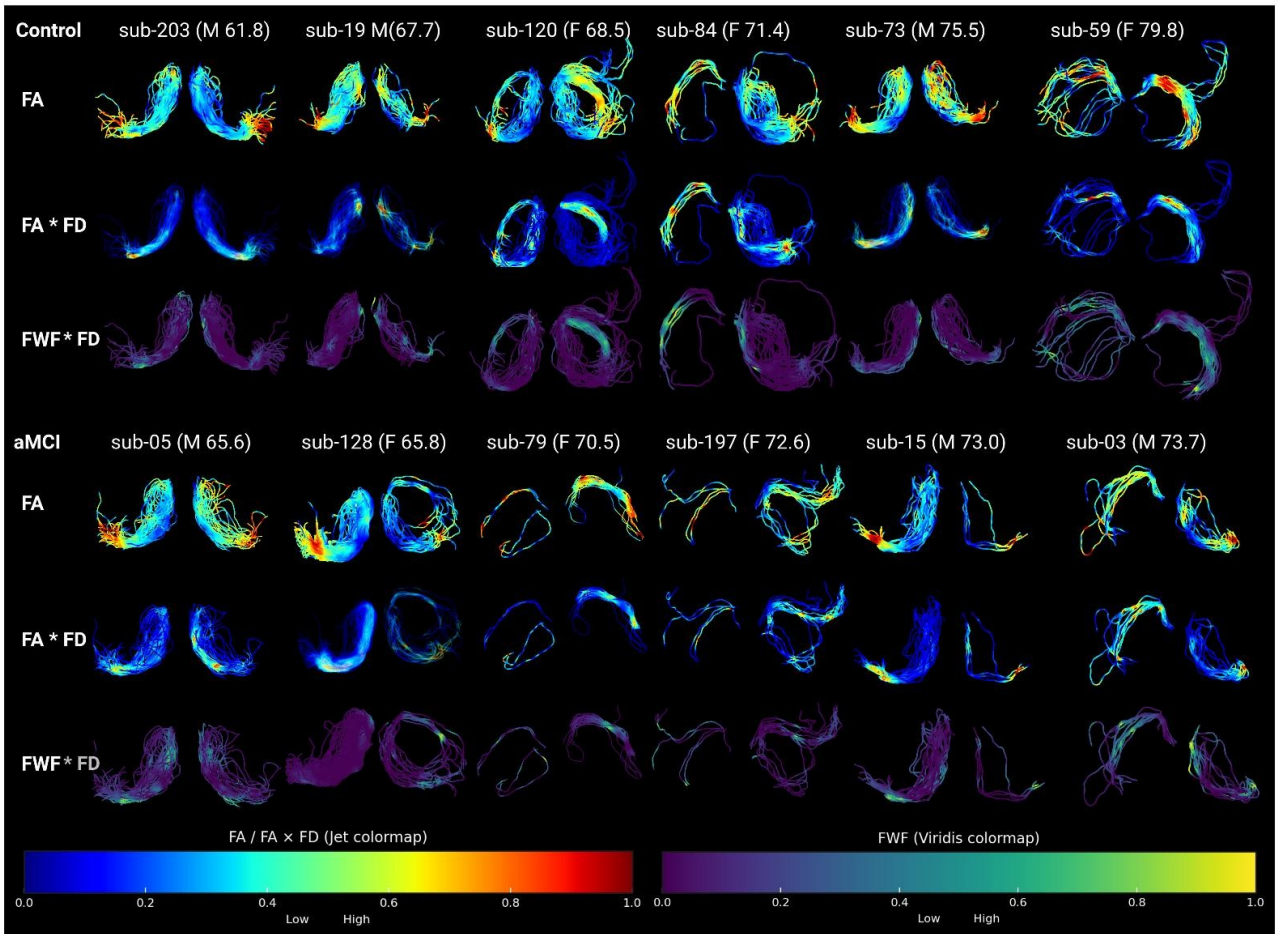

*Figure 10: Tractography reconstructions of the Re–hippocampal tract are shown for 6 representative participants from each group, **top**: Control; **bottom**: aMCI = amnestic mild cognitive impaired.. Each column displays streamlines from one subject, colour-coded by three microstructural indices: **top rows**: FA , **middle rows**: FA × FD, **bottom rows**: FWF. Warmer colours indicate higher values (red/yellow), while cooler tones represent lower values (blue/purple). Age and gender are indicated above each column (M: male, F: female). In select cases, semi-transparent rendering was used to emphasise the core structure of the tract.*

3.6 Reduced fibre density of reuniens-hippocampal tract in aMCI

Figure 11 displays the group-level distribution of mean fibre density (Control vs. aMCI), separated by hemisphere. The aMCI group shows very strong evidence for lower fibre density values compared to the control group. (P+ = 0.0199).

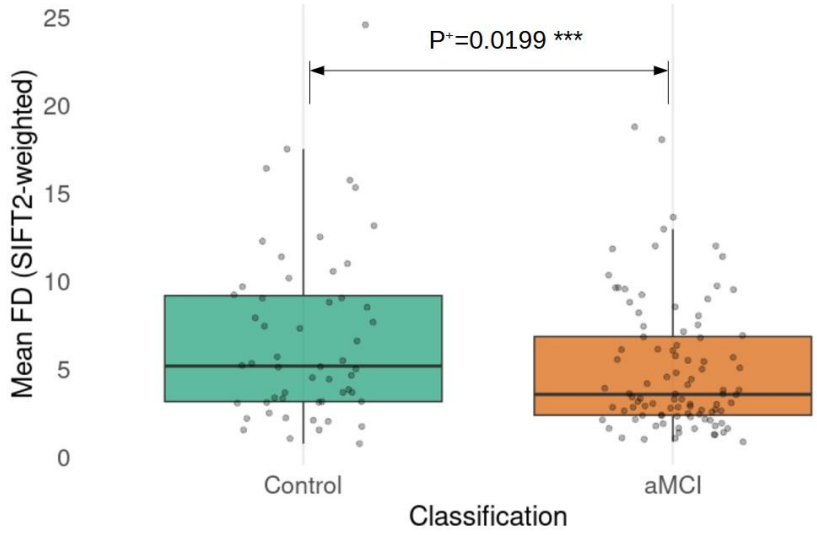

*Figure 11: Boxplot of SIFT2-weighted mean fibre density per tract, separated by classification. aMCI = amnestic mild cognitive impairment, FD = fibre density, SIFT2 = spherically informed filtering of tractogram 2, P+ = positive posterior probability. *** = very strong evidence.*

4. Discussion

4.1 Summary and interpretation of findings

Differences in white matter integrity of the nucleus reuniens–hippocampus tract were examined in aMCI patients compared to healthy controls. Using tract-specific DTI and NODDI dMRI metrics and SIFT2-weighted connectivity measures, the main findings of the study were: 1) the method successfully selected streamlines connecting the reuniens and hippocampal area; 2) mean fractional anisotropy was increased in aMCI in the unweighted voxel-based method, while mean free water fraction and orientation dispersion index were increased in the SIFT2-informed method; 3) the SIFT2-informed mean fibre density of the tract was reduced in aMCI compared to controls; and 4) reuniens and hippocampal segmented areas were smaller and ventricles were enlarged in the aMCI group, but differences could be attributed to gender.

4.2 Tract anatomy and reconstruction

Tractography successfully identified streamlines between the reuniens and hippocampal subregions in all participants. Compared to controls, the aMCI group showed weak evidence for a reduced number of streamlines, strong evidence for enlarged lateral and third ventricle volumes and very strong evidence for smaller ROI volumes in both the hippocampus and Re. Visually, streamlines in the

aMCI group appeared more fragmented and more often followed an anterior path. It is important to note that an incomplete or fragmented tractography reconstruction does not mean that the biological pathway is entirely absent or severed. More often it reflects reduced anisotropy in that region—commonly due to age- or disease-related microstructural changes—which causes the tracking algorithm to stop. This is relevant in conditions like aMCI, where subtle degeneration may lower FA values below the threshold for tract continuation. Similar patterns were observed by (Shaikh et al., 2022), who reported more dispersed and less coherent tractography in the fornix of aMCI patients, likely reflecting early but incomplete tract disruption.

The main trajectory of the reconstructed tract showed a characteristic posterior curvature similar to the path of the fornix; a C-shaped white matter bundle connecting the hippocampus to subcortical structures, arching over the thalamus and along the lateral ventricle, see Figure 12. The fornix is a key component of the limbic system and plays a critical role in memory; damage to this structure is associated with severe episodic memory deficit (Aggleton et al., 2000; Vann et al., 2008). It is thus highly plausible that the reuniens–hippocampal tract follows this route.

However, the emergence of anteriorly deviating streamlines is less straightforward. No anterior Re–hippocampal tract has been described in anatomical studies to date. One hypothesis is that these streamlines may reflect geometric alterations in white matter orientation due to ventricular enlargement. In Alzheimer's disease, lateral ventricle dilation is common and has been associated with local changes in white matter geometry (Zhao et al., 2021). Although these effects are more subtle in aMCI, minor orientation changes near the ventricular wall could theoretically shift trajectories. In the context of compensatory plasticity (Torrealba et al., 2023), it is conceivable that the brain might attempt to reroute information flow along alternative paths. However, given that diffusion MRI reflects structural, not functional, connectivity—and that only minor geometric changes were observed in aMCI—this interpretation remains speculative.

A more plausible explanation involves methodological limitations due to the small – and in aMCI reduced – Re volume. As the Re shrinks in aMCI, segmentation becomes less precise, particularly since segmentations were derived from high-resolution T1-weighted images (1 mm^3), while tractography was performed on lower-resolution DWI data (2 mm^3). This resolution mismatch increases the likelihood of partial volume effects, whereby voxels may contain signal from adjacent thalamic nuclei or white matter bundles.

Moreover, our selection criteria may have further contributed to the selection of false positive streamlines. Specifically, the Re segmentation was dilated by two voxels in T1 space to prevent the spatial information being lost in the trasform to DWI space. In addition, streamlines were included if their endpoints lay within a 2 mm radius of the resulting mask, i.e. the 'local search' method. While

this approach increases sensitivity, it also elevates the risk of incorporating fibres not originating or terminating in the Re.

While no thalamic nuclei projections have been described following an anterior lateral path, a structure just anterior of the thalamus is the anterior commissure, a midline fibre bundle with lateral projections to subcortical regions including the entorhinal cortex (Guenot, 1998; Rayboud, 2010), Since the entorhinal cortex was included in our hippocampal area mask, streamlines from this region may be mistakenly assigned as connecting to Re. This could result in anatomically plausible but unintended anterior routes, particularly when the Re becomes too small or imprecisely segmented to attract streamlines. Thus, while these anterior deviations probably do not indicate a novel anatomical pathway, they may reflect tractography artifacts due to regional atrophy and registration mismatch.

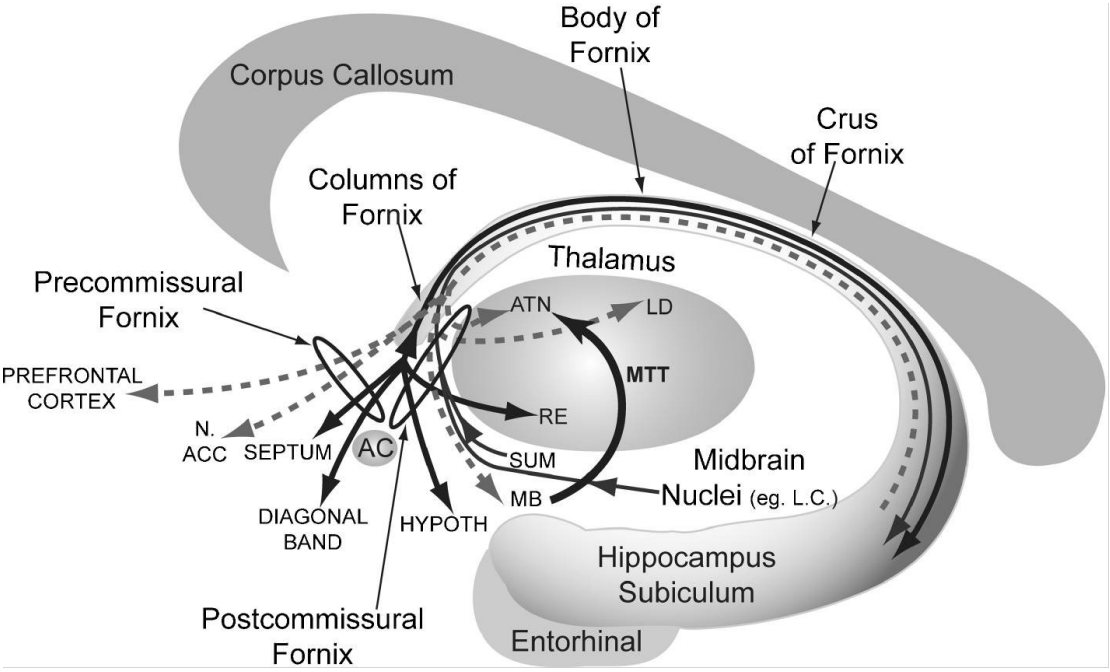

Figure 12: Diagrammatic representation of the location of the fornix and its divisions from (Aggleton et al., 2010). The dashed arrows show fornical connections that are solely efferent from the hippocampal formation, the narrow, solid arrows show fornical connections that are solely afferent to the hippocampal formation, and the wide, solid arrows show reciprocal connections within the fornix. Abbreviations: AC, anterior commissure; ATN, anterior thalamic nuclei; HYPOTH, hypothalamus; LC, locus coeruleus; LD, thalamic nucleus lateralis dorsalis; MB, mammillary bodies; RE, nucleus reuniens; SUM, supramammillary nucleus

4.3 Group differences in diffusion metrics: unweighted analysis

In the standard voxel-averaged analysis of the TOI, moderate evidence was found for increased FA, weak evidence for reduced RD and anecdotal evidence for reduced ADC and ODI in aMCI participants. Moreover, no consistent group differences were observed for AxD, NDI, FWF. This deviates from our initial hypothesis, which predicted reduced FA and NDI alongside elevated RD, ODI, and FWF in aMCI.

FA is commonly interpreted as a marker sensitive to axonal integrity, with reduced values suggesting axonal degeneration. RD is thought to reflect myelin integrity and axonal packing, while ADC is more broadly sensitive to changes in tissue composition such as necrosis (Alexander et al., 2011; Racin et al., 2014). An elevated FA could therefore be interpreted as preserved axonal structure, a reduced RD as more axonal density and a reduced ADC as less necrotic tissue. However, Alzheimer's disease is associated with white matter damage, including demyelination and axonal degeneration (Nasrabady et al., 2018; Wen et al., 2021). Therefore, the observed FA increase may instead reflect something else.

One explanation could be a neuroinflammatory response caused by the disease. In particular, glial activation in early AD stages can restrict water diffusion by increasing cellularity and decreasing extracellular space, resulting in artificially elevated FA values (Benitez et al., 2022). Supporting this, other studies have documented a non-linear relationship between amyloid load and diffusion measures: initial amyloid deposition may increase FA and reduce diffusivity, whereas later-stage pathology reverses this pattern (Collij et al., 2021; Racin et al., 2014; Wolf et al., 2015).Thus, our findings may capture an early-stage, gliosis/amyloid-associated phase of microstructural remodelling, potentially preceding later white matter loss.

A complementary explanation is a survivorship bias. The iFOD2 algorithm (see Figure 2) used in this study favours pathways with high directional certainty. In aMCI participants, where white matter integrity may already be compromised, this results in preferential reconstruction of only the most coherent fibre segments—those with higher FA. The less coherent or damaged regions with low FA are less likely to be traversed. As a consequence, damaged or ambiguous tract regions may be excluded from the TOI, artificially inflating the mean FA. This survivorship bias means that reconstructed tracts in aMCI may represent only a preserved subset of the pathway, skewing group-level comparisons toward higher integrity.

This bias may be further amplified by anatomical differences: in this study, the hippocampal ROI was smaller in the aMCI group compared to controls, which could reduce the number of streamlines terminating in the target region. Since streamlines that do not reach the ROI are excluded from the TOI, the reconstructed tract in aMCI may represent only a fraction of the original bundle—likely those that are more structurally preserved. Thus, since the streamlines already underwent a different selection process per classification, the remaining TOI could give an illusion of higher FA and tract coherence in aMCI than truly exists.

4.4 Group differences in SIFT2-weighted metrics

Interestingly, the pattern of results shifted after applying SIFT2 informed weights. This second analysis revealed moderate evidence for increased FWF and ODI in participants with aMCI and no evidence for a difference between groups in the other metrics. These findings better align with our initial hypothesis.

FWF reflects the proportion of isotropic diffusion, mainly CSF, but freely diffusing water molecules are also increased by myelin damage in neurodegenerative disorders (S. S. Wang et al., 2018). While a high FWF may simply reflect anatomical proximity to CSF-filled spaces, it can also signal pathological processes such as inflammation, edema, or tissue loss. Animal models of AD have shown that changes in FWF correspond to the evolution of neuroinflammatory responses (Fick et al., 2016). Also, elevated FWF has been reported in aMCI before (Fu et al., 2023). These findings support the interpretation of increased FWF in aMCI as a marker of early pathological processes.

ODI reflects the angular variability of fibre orientations and is often used to infer microstructural features such as axonal disorganisation. Gozdas et al., (2021) found that an increase in ODI indicates axonal damage and demyelination and a meta-analysis by Zhong et al,. (2023) showed increased white matter ODI values in patients with MCI and AD, all supporting our hypothesis and current findings in the reuniens-hippocampal tract.

SIFT2 weighting uses the underlying FOD to assign biologically informed weights to streamlines, allowing more plausible fibres to contribute more strongly to the metric estimation. By including these weights in our model, streamlines traversing noisy or implausible FOD regions—those responsible for high but anatomically questionable FA—are down weighted. Meanwhile, streamlines passing through denser and more biologically plausible white matter pathways are upweighted. The result is a tract profile that better reflects the “core” structural connection between the nucleus reuniens and hippocampus (see Figure 10) and that aligns more closely with expected microstructural changes in aMCI.

This improved anatomical specificity is further supported by our finding of reduced SIFT2-informed fibre density in the aMCI group. Very strong Bayesian evidence indicated that fibre density, calculated from the summed SIFT2 weights of streamlines within the tract, was lower in aMCI participants compared to controls. As this measure serves as a proxy for structural connectivity strength, it may reflect true anatomical disconnection or axonal degeneration within the Re–hippocampal tract. This interpretation is in line with previous studies documenting reduced fibre density the fornix in AD (Mito et al., 2018). Nevertheless, it is important to note that fibre density remains a model-based estimate and should be interpreted alongside conventional metrics and anatomical constraints.

Taken together, the SIFT2-weighted approach yielded diffusion profiles that better matched the expected pathological changes, by downweighting anatomically implausible streamlines and emphasising those aligned with local FODs. Although histological validation is lacking, these findings suggest that FOD-informed weighting schemes can enhance sensitivity to group differences, particularly in clinical or ageing populations. Compared to unweighted analyses, this approach likely provides a more biologically meaningful estimate of microstructural differences.

4.5 Methodological considerations

It is important to consider several methodological limitations when using diffusion MRI. Metrics derived from DTI are inherently relative and can be affected by numerous other factors. This may help explain why no robust group differences were found in the SIFT2 weighted DTI metrics between aMCI participants and controls. As illustrated in Figure 13, changes in FA do not always reflect actual tissue loss: when crossing fibres degrade asymmetrically, FA can paradoxically increase (Figure 13A); and when all fibre populations are equally affected, FA may remain stable despite tissue damage (Figure 13B). Such examples underscore that FA may be insensitive to subtle or local neurodegeneration, as is likely the case in early-stage aMCI (see also Figley et al., (2022)).

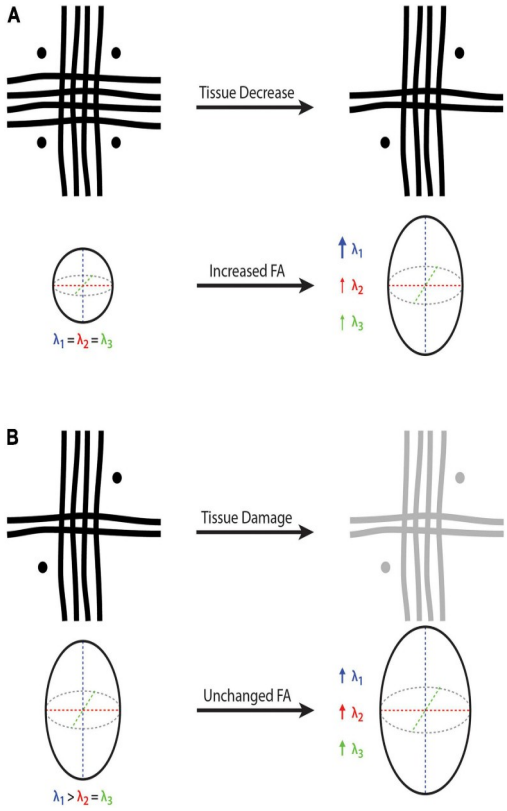

Figure 13: Cartoon by Figley et al., (2022) is a representation of how tissue loss in regions with crossing fibres can alter diffusion tensor eigenvalues and fractional anisotropy (FA), adapted from Figley et al. (2022). (A) Uneven fibre loss leads to a dominant direction and increased FA, despite overall tissue loss. (B) Uniform degradation across fibre populations leads to unchanged FA. The figure illustrates how FA can misrepresent underlying pathology in complex fibre configurations.

Another key limitation of DTI is its susceptibility to partial volume effects, particularly contamination from cerebrospinal fluid (CSF), which is common in periventricular regions like the fornix. In voxels partially occupied by CSF, the microstructural parameters (e.g., FA, MD) are confounded, leading to potential underestimation or overestimation of diffusion properties (Pierpaoli & Basser, 1996). This issue is relevant in our study, where the SIFT2-weighted analysis revealed increased FWF in aMCI participants. To address this issue, Pasternak et al. (2009) proposed a free water (FW) elimination model, FW-DTI which estimates and removes the extracellular free water signal to improve the specificity of DTI-derived measures.

Beyond DTI, NODDI modelling provides a more biologically informed framework by separately estimating tissue compartments. Importantly, the NDI and ODI are designed to be insensitive to CSF

contamination, offering improved robustness in regions affected by ventricular enlargement. However, this does not make NODDI immune to partial volume effects. As shown by Parker et al. (2021), computing mean NDI or ODI values across an ROI, without accounting for the variable tissue fraction (after removal of CSF) per voxel, can lead to biased estimates. This is particularly problematic in ROIs with substantial CSF intrusion, such as the periventricular white matter tracts bordering the lateral ventricles—precisely where degeneration and atrophy are prominent in Alzheimer's disease (Iglesias et al., 2018). To solve this issue, voxel-wise modelling with explicit CSF correction has been proposed by (Bergamino et al., 2021).

The FWF estimated by NODDI is often interpreted as a proxy for extracellular CSF content, simply reflecting proximity to CSF-filled spaces, or reflecting pathological processes such as inflammation, edema, or tissue loss (see Section 4.4). This dual interpretation complicates the use of FWF as a clean measure of pathology, especially in patient populations with enlarged ventricles.

From a statistical standpoint, a better practice would be to incorporate streamline-level information directly into the Bayesian model, as this retains more of the original data structure and variability. Although such an approach would ideally allow each streamline's metric and SIFT2-derived weight to contribute proportionally, we were unable to implement this in our current Bayesian framework. Therefore, we opted to summarise tract profiles as weighted means per subject and hemisphere. While this approach allows for group-level comparisons, future models that include streamline-wise inputs could more accurately reflect the richness and variability of the underlying tract data.

In summary, interpreting diffusion metrics in periventricular tracts like the Re–hippocampal pathway requires caution due to several methodological constraints. DTI-based measures such as FA and MD are relative, non-specific, and susceptible to partial volume effects. In our study, elevated FWF underscores the evidence this last bias, which could reflect either extracellular CSF accumulation or early pathological processes. While NODDI offers improved specificity by modelling distinct tissue compartments, it is sensitive to voxel-wise CSF proportions unless corrected. Recent methods like FW-DTI and CSF-corrected NODDI provide promising solutions, though they come with added complexity. We mitigated these challenges through the use of ACT, automated ROI segmentation, and biologically informed SIFT2 weighting. Still, residual confounds persist, especially in regions bordering the third and lateral ventricles. Despite these limitations, the observed increases in FWF and ODI likely reflect early-stage microstructural changes, supporting the Re–hippocampal tract as a sensitive marker of prodromal Alzheimer's disease

4.6 Gender-related confounding effects

The unequal gender distribution between the aMCI and control groups, with a higher proportion of females in the control group, may have introduced confounding effects. Anatomical and clinical sex

differences are well documented: women typically have smaller lateral ventricles than men, even when accounting for intracranial volume (Kaye et al., 1992). Clinically, sex also moderates disease progression—female patients with MCI tend to exhibit faster cognitive and functional decline than their male counterparts (Lin et al., 2015). In our gender-stratified post hoc analysis, third ventricle volume differences appeared to reflect both gender and diagnostic classification. Future studies should therefore aim to match groups by sex or include the interaction effect of sex to avoid potential confounding effects.

4.7 Integration with Alzheimer's pathophysiology

The observed changes span multiple levels of pathology: increased free water and orientation dispersion at the cellular level; reduced Re and hippocampal volumes and ventricular enlargement at the regional level; and reduced fibre density at the network level. Together, these alterations are consistent with early features of Alzheimer's disease and support the interpretation that tract degeneration may be an early marker of disease progression. Moreover, because the Re links the medial prefrontal cortex and hippocampus—two key hubs within the memory-supporting Papez circuit (see Section 1.3)—its disruption may contribute directly to the episodic memory impairments observed in aMCI.

Importantly, the reuniens-hippocampal tract is not only structurally altered but is also functionally relevant to Alzheimer's symptoms. Rodent studies have shown that projections from the mPFC to the Re and perirhinal cortex support distinct memory retrieval strategies (Jayachandran et al., 2019), and that silencing mPFC → Re pathways impairs sequence memory. Moreover, optogenetic stimulation of Re neurons modulates memory specificity and generalisation (Xu & Sudhof, 2013), while lesions or inhibition of the Re disrupt associative learning (Eleore et al., 2011). These findings highlight the involvement of the Re in memory, making it a plausible target of early AD-related disruption.

The altered tract profile observed by the weighted analysis—marked by elevated FWF and ODI—aligns with pathological processes such as inflammation, dendritic disorganisation, and axonal demyelination, all of which have been implicated in early Alzheimer's disease (Bartzokis, 2011; Heneka et al., 2015; Spires-Jones & Hyman, 2014). These results suggest that biologically informed weighting approaches can enhance sensitivity to early microstructural changes.

Finally, this approach may help identify structural disconnection in the reuniens–hippocampal tract even before gray matter atrophy becomes apparent. Although the present study did reveal reduced segmentation volumes in both the reuniens and hippocampus, it cannot distinguish between true atrophy and displacement due to ventricular expansion, nor can it provide histological validation. Notably, Censi et al. (2024) have already reported reuniens atrophy at the aMCI stage, supporting the view that this structure is affected early in the disease process. However, this also means we cannot

determine whether gray matter atrophy preceded white matter degeneration in this pathway, or vice versa. Longitudinal studies are therefore needed to clarify the temporal sequence of microstructural and morphological changes. Nonetheless, the convergence of diffusion- and volume-based alterations in this pathway supports the hypothesis that reuniens–hippocampal tract alterations are early features of aMCI and may serve as a promising target for further investigation.

4.8 Future directions

Strength of this research are combing the most advanced tractography tools in subject-specific space to accurately isolate the reuniens-hippocampal tract, an understudied but functionally critical connection in memory networks. By comparing conventional voxel-based metrics with SIFT2-weighted alternatives, we offer a biologically informed method that improves sensitivity to early microstructural changes. The use of both DTI and NODDI further strengthens interpretability by disentangling diffusion changes related to axonal damage, dispersion, and free water. Together, these choices increase anatomical precision and relevance to Alzheimer's pathology.

This study has several limitations. The control group was predominantly female, introducing potential gender-related bias. Only one tractography algorithm with fixed parameters was used, limiting methodological generalisability. Atlas-based segmentation of small nuclei like the reuniens may be imprecise, particularly in ageing brains with structural variability. The cross-sectional design offers only a single snapshot in time, limiting causal inference about disease progression. Lastly, although the NODDI model reduces CSF contamination, partial volume effects may still influence diffusion estimates and complicate interpretation in periventricular tracts.

Future directions can expand on the current findings. First, combining tractography with functional measures, such as correlating fibre metrics with BOLD signals, could illuminate functional–structural coupling in the Re–hippocampal tract. High-resolution imaging (e.g., 7Tesla MRI or multi-band acquisition) may improve delineation of small nuclei and minimise partial volume effects. Longitudinal studies tracking Re–hippocampal tract properties over time, especially in individuals converting from aMCI to Alzheimer's, would offer stronger insights into disease progression. Finally, methodological refinements such as dual-seed tractography (e.g., including the anterior commissure) could enhance biological specificity. Future work could also examine differential Re connectivity to hippocampal subfields (e.g., CA1 vs. subiculum), as these may show distinct patterns of vulnerability.

4.9 Conclusion

This study provides novel evidence that the reuniens–hippocampal tract is structurally altered in individuals with aMCI, a condition considered prodromal to Alzheimer's disease. Using anatomically

constrained tractography, we were able to successfully reconstruct this tract in all participants, demonstrating the feasibility of studying this under explored connection in vivo.

By combining standard and SIFT2-weighted diffusion models, we captured subtle microstructural changes that might otherwise be obscured. Our multimodal approach, integrating DTI and NODDI, allowed us to disentangle axonal damage, orientation dispersion, and free water accumulation.

The findings spread across multiple levels. At the cellular level, increased FWF and ODI suggest inflammation-related and dispersion-driven changes. At the regional level, reduced reuniens and hippocampal segmented volumes and ventricular expansion reflect anatomical changes. At the network level, decreased fibre density in the SIFT2-weighted analysis indicates structural disconnection within the memory-critical Papez circuit.

Interestingly, FA was elevated in the unweighted analysis, a counter-intuitive finding that may reflect early gliosis or. More plausibly, survivorship bias in streamline reconstruction. This highlights the importance of weighted models for generating more biologically meaningful tract profiles.

Together, these results support the hypothesis that white matter degeneration in the Re–hippocampal tract may be an early and sensitive marker of AD-related pathology. While histological validation and longitudinal imaging remain essential, this tract shows promise as a target for early detection and monitoring of disease progression.

Acknowledgements

I would like to thank Professor Dr. I. Kirk for making it possible for me to come to New Zealand in the first place, for his trust and support throughout this project and for the time he always took to engage with my work. The freedom he gave me to explore made a big difference and allowed me to develop the project independently.

I am also very grateful to my daily supervisor, Dylan Taylor, for his valuable insights into doing good research, his practical advice (sometimes not asked for, but always very helpful), and for always being available to discuss my approach, results and interpretations.

Thanks as well to Professor Dr. M. M. Lorist for her willingness to think along, her support, and her enthusiasm for this project. Also, I am grateful to Nikki Dreijer for introducing me to this research group.

I would also like to thank the MSc BCN programme for encouraging international research experiences, and the Marco Polo Fund for providing financial support. Special thanks to my study

coordinators, Dr. Mark Nieuwenstein and Dr. Tassos Sarampalis, for always thinking along and helping to find solutions to make this project possible.

I'm proud of what I've achieved, but I could not have done it without the help of these and other colleagues, both in New Zealand and in the Netherlands.

5 References

Aggleton, J. P., McMackin, D., Carpenter, K., Hornak, J., Kapur, N., Halpin, S., Wiles, C. M., Kamel, H., Brennan, P., & Gaffan, D. (2000). Differential effects of colloid cysts in the third ventricle that spare or compromise the fornix. *Brain*, *123*, 800–815. https://doi.org/10.1093/brain/123.4.800

Aggleton, J. P., O'Mara, S. M., Vann, S. D., Wright, N. F., Tsanov, M., & Erichsen, J. T. (2010). Hippocampal-anterior thalamic pathways for memory: Uncovering a network of direct and indirect actions. *The European Journal of Neuroscience*, *31*(12), 2292–2307. https://doi.org/10.1111/j.1460-9568.2010.07251.x

Agosta, F., Pievani, M., Sala, S., Geroldi, C., Galluzzi, S., & Frisoni, G. B. (2011). White matter damage in Alzheimer Disease and its relationship to gray matter atrophy. *Radiology*, *258*, 853–863. https://doi.org/10.1148/radiol.10101284

Alexander, A. L., Hurley, S. A., Samsonov, N., Hosseinbor, P., Mossahebi, P. M., Tromp do, E., & Field, A. S. (2011). Characterization of cerebral white matter properties using quantitative magnetic resonance imaging stains. *Brain Connectivity*, *1*(6), 423–446. https://doi.org/10.1089/brain.2011.0071

Alzheimer, A., Stelzmann, R. A., Schnitzlein, H. N., & Murtagh, F. R. (1995). An English translation of Alzheimer's 1907 paper, "Uber eine eigenartige Erkankung der Hirnrinde. *Clinical Anatomy*, *8*, 429–431. https://doi.org/10.1002/ca.980080612

Amlien, I. K., & Fjell, A. M. (2014). Diffusion tensor imaging of white matter degeneration in Alzheimer's disease and mild cognitive impairment. *Neuroscience*, *276*, 206–215. https://doi.org/10.1016/j.neuroscience.2014.02.017

Andersson, J. L. R., Skare, S., & Ashburner, J. (2003). How to correct susceptibility distortions in spin-echo echo-planar images: Application to diffusion tensor imaging. *NeuroImage*, *20*, 870–888. https://doi.org/10.1016/S1053-8119(03)00336-7

Andersson, J. L. R., & Sotiropoulos, S. N. (2016). An integrated approach to correction for off- resonance effects and subject movement in diffusion MR imaging. *NeuroImage*, *125*, 1063–1078. https://doi.org/10.1016/j.neuroimage.2015.10.019

Augustinack, J. C., Huber, K. E., Stevens, A. A., Roy, M., Frosch, M. P., van der Kouwe, A. J. W., Wald, L. L., van Leemput, K., McKee, A. C., & Fischl, B. (2013). Predicting the location of human perirhinal cortex, Brodmann's area 35, from MRI. *NeuroImage*, *1*(64), 32–42. https://doi.org/10.1016/j.neuroimage.2012.08.071

Bartzokis, G. (2011). Alzheimer's disease as homeostatic responses to age-related myelin breakdown. *Neurobiology of Aging*, *32*(8), 1341–1371. https://doi.org/10.1016/j.neurobiolaging.2009.08.007

Basser, P. J., Mattiello, J., & LeBihan, D. (1994). MR diffusion tensor spectroscopy and imaging. *Biophysiology Journal*, *66*, 259–267. https://doi.org/10.1016/S0006-3495(94)80775-1

Benitez, A., Jensen, J. H., Thorn, K., Dhiman, S., Fountain-Zaragoza, S., Rieter, W. J., Spampinato, M. V., Hamlett, E. D., Nietert, P. J., Falangola, M. F., & Helpern, J. A. (2022). Greater Diffusion Restriction in White Matter in Preclinical Alzheimer Disease. *Annals of Neurology*, *91*(6), 864–877. https://doi.org/10.1002/ana.26353

Bergamino, M., Walsh, R. R., & Stokes, A. M. (2021). Free-water diffusion tensor imaging improves the accuracy and sensitivity of white matter analysis in Alzheimer's disease. *Scientific Reports*, *11*(1). https://doi.org/10.1038/s41598-021-86505-7

Bokde, A. L. W., Ewers, M., & Lebihan, D. (2009). Assessing neuronal networks: Understanding Alzheimer's disease. *Progress in Neurobiology*, *89*, 125–133. https://doi.org/10.1016/j.pneurobio.2009.06.004 PMID:

Braak, H., & Braak, E. (1991a). Alzheimer's disease affects limbic nuclei of the thalamus. *Acta Neuropathologica*, *81*, 261–268. https://doi.org/10.1007/BF00305867

Braak, H., & Braak, E. (1991b). Demonstration of amyloid deposits and neurofibrillary changes in whole brain sections. *Brain Pathology*, *1*(3), 213–216. https://doi.org/10.1111/j.1750-3639.1991.tb00661.x

Braak, H., & Braak, E. (1991c). Neuropathological stageing of Alzheimer-related changes. *Acta Neuropathologica*, *82*, 239–259. https://doi.org/10.1007/bf00308809

Bubb, E. J., Kinnavane, L., & Aggleton, J. P. (2017). Hippocampal—Diencephalic—Cingulate networks for memory and emotion: An anatomical guide. *Brain Neuroscience Advances*, *1*(1). https://doi.org/10.1177/2398212817723443

Buckner, R. L., Head, D., Parker, J., Fotenos, A. F., Marcus, D., Morris, J. C., & Snyder, A. Z. (2004). A unified approach for morphometric and functional data analysis in young, old, and demented adults using automated atlas-based head size normalization: Reliability and validation against manual measurement of total intracranial volume. *NeuroImage*, *23*(2), 724–738. https://doi.org/10.1016/j.neuroimage.2004.06.018

Burkner, P. C. (2017). brms: An R Package for Bayesian Multilevel Models using Stan. *Journal of Statistical Software*, *80*(1), 1–28. https://doi.org/10.18637/jss.v080.i01

Burkner, P. C. (2018). Advanced Bayesian Multilevel Modeling with the R Package brms. *The R Journal*, *10*(1), 395–411. https://doi.org/10.32614/RJ-2018-017

Calamante, F., Tournier, J.-D., Jackson, G. D., & Connelly, A. (2010). Track-density imaging (TDI): Super-resolution white matter imaging using whole-brain track-density mapping. *NeuroImage*, *53*, 1233–1243. https://doi.org/10.1016/j.neuroimage.2010.07.024

Carpenter, B., Gelman, A., Hoffman, M. D., Lee, D., Goodrich, B., Betancourt, M., Brubaker, M., Guo, J., Li, P., & Riddel, A. (2017). Stan: A probabilistic programming language. *Journal of Statistical Software*, *76*(1). https://doi.org/10.18637/jss.v076.i01

Censi, S., Sestieri, C., Punzy, M., Delli Pizzi, A., Ferretti, A., Gambi, F., Tomassini, V., Delli Pizzi, S., & Sensi, S. L. (2024). "Back to Braak": Role of Nucleus Reuniens and Subcortical Pathways in Alzheimer's Disease Progression. *Journal of Prevention of Alzheimer's Disease*, *11*(4), 1030–1040. https://doi.org/10.14283/jpad.2024.42

Chen, G., Xiao, Y., Taylor, P. A., Rajendra, J. K., Riggins, T., Geng, F., Redcay, E., & Cox, R. W. (2019). Handling multiplicity in neuroimaging through Bayesian lenses with multilevel modeling. *Neuroinformatics*, *17*. https://doi.org/10.1007/s12021-018- 9409-6

Collij, L. E., Ingala, S., Top, H., Wottschel, V., Stickney, K. E., Tomassen, J., Konijnenberg, E., Ten Kate, M., Sudre, C., Alves, I. L., Yaqub, M. M., Wink, A. M., Ent, D. V., Scheltens, P., Bercek, B. N. M., Visser, P. J., Barkhof, F., & Den Braber, A. (2021). White matter microstructure disruption in early stage amyloid pathology. *Alzheimer's & Dementia: Diagnosis, Assessment & Disease Monitoring*, *13*(1). https://doi.org/10.1002/dad2.12124

Daducci, A., Canales-Rodriguez, E. J., Zhang, H., Dyrby, T. B., Alexander, D. C., & Thiran, J.-P. (2015). Accelerated Microstructure Imaging via Convex Optimization (AMICO) from diffusion MRI data. *NeuroImage*, *105*, 32–44. https://doi.org/10.1016/j.neuroimage.2014.10.026

Daducci, A., Marigonda, A., Orlandi, G., & Posenato, R. (2012). Neuronal Fiber–tracking via optimal mass transportation. *Communications on Pure and Applied Analysis*, *11*, 2157. https://doi.org/10.3934/cpaa.2012.11.2157

Desikan, R. S., Segonne, F., Fischl, B., Quinn, B. T., Dickerson, B. C., Blacker, D., Buckner, R. L., Dale, A. M., Maguire, R. P., Hyman, B. T., Albert, M. S., & Killiany, R. J. (2006). An automated labeling system for subdividing the human cerebral cortex on MRI scans into gyral based regions of interest. *NeuroImage*, *31*(3), 968–980. https://doi.org/10.1016/j.neuroimage.2006.01.021

Dhollander, T., Raffelt, D., & Connelly, A. (2016). *Unsupervised 3-tissue response function estimation from single-shell or multi-shell diffusion MR data without a co-registered T1 image*. *pp. 5*.

Dhollander, T., Tabbara, R., Rosnarho-Tornstrand, J., Tournier, J.-D., Raffelt, D., & Connelly, A. (2021). *Multi-tissue log-domain intensity and inhomogeneity normalisation for quantitative apparent fibre density*. *29*, 2472.

Eleore, L., Lopez-Ramos, J. C., Guerra-Narbona, R., & Delgado-Garcia, J. M. (2011). Role of Reuniens Nucleus Projections to the Medial Prefrontal Cortex and to the Hippocampal Pyramidal CA1 Area in Associative Learning. *PLoS ONE*, *6*(8). https://doi.org/10.1371/journal.pone.0023538

Fick, R. H. J., Daianu, M., Pizzolato, M., Wassermann, D., Jacobs, R. E., & Thompson, P. M. (2016). Comparison of biomarkers in transgenic Alzheimer rats using multi-shell diffusion MRI. In *Computational Diffusion MRI: MICCAI Workshop* (pp. 187–199). Springer.

Figley, C. R., Uddin, M. N., Wong, K., Kornelsen, J., Puig, J., & Figley, T. D. (2022). Potential pitfalls of using fractional anisotropy, axial diffusivity, and radial diffusivity as biomarkers of cerebral white matter microstructure. *Frontiers in Neuroscience*, *15*. https://doi.org/10.3389/fnins.2021.799576

Fischl, B. (2012). FreeSurfer. *NeuroImage*, *62*(2), 774–781. https://doi.org/10.1016/j.neuroimage.2012.01.021

Fischl, B., Salat, D. H., Busa, E., Albert, M., Dieterich, M., Haselgrove, C., van der Kouwe, A., Killiany, R., Kennedy, D., Klaveness, S., Montillo, A., Makris, N., Rosen, B., & Dale, A. M. (2002). Whole Brain Segmentation. *Neurotechnique*, *33*(3), 341–355. https://doi.org/10.1016/s0896-6273(02)00569-x

Fletcher, E., Raman, M., Huebner, P., Liu, A., Mungas, D., & Carmichael, O. (2013). Loss of fornix white matter volume as a predictor of cognitive impairment in cognitively normal elderly individuals. *JAMA Neurology*, *70*, 1389–1395. https://doi.org/10.1001/jamaneurol.2013.3263

Fu, X., Wang, X., Zhang, Y., Li, T., Tan, Z., Chen, Y., Zhang, X., & Ni., H. (2023). Brain Microstructural Changes in Patients with Amnestic mild Cognitive Impairment. *Clinical Neuroradiology*, *33*, 445–453. https://doi.org/10.1007/s00062-022-01226-2

Gauthier, S., Reisberg, B., Zaudig, M., Petersen, R. C., Ritchie, K., & Broich, K. (2006). Mild cognitive impairment. *Lancet*, *367*, 1262–1270. https://doi.org/10.1016/S0140-6736(06)68542-5

Gilligan, T. M., Sibilia, F., Farrell, D., Lyons, D., Kennelly, S. P., & Bokde, A. L. W. (2019). No relationship between fornix and cingulum degradation and within-network decreases in functional connectivity in prodromal Alzheimer's disease. *Public Library of Science One*, *14*(10), Article 10. https://doi.org/10.1371/journal.pone.0222977

Gozdas, E., Fingerhut, H., Dacorro, L., Bruno, J. L., & Hosseini, S. M. (2021). Neurite imaging reveals widespread alterations in gray and white matter neurite morphology in healthy aging and amnestic mild cognitive impairment. *Cerebral Cortex*, *31*, 5570–5578. https://doi.org/10.1093/cercor/bhab180

Guenot, M. (1998). Transfert interhemispherique et agenesie du corps calleux. Capacites et limites de la commissure blanche anterieure. *Neurochirurgie*, *44*(Suppl 1), 113–115.
Hardy, J., & Selkoe, D. J. (2002). Medicine—The amyloid hypothesis of Alzheimer's disease: Progress and problems on the road to therapeutics. *Science*, *297*(5580), 353–356.
Heneka, M. T., Carson, M. J., El Khoury, J., Landreth, G. E., Brosseron, F., Feinstein, D. L., Jacobs, A. H., Wyss-Coray, T., Vitorica, J., Ransohoff, R. M., Herrup, K., Frautschy, S. A., Finsen, B., Brown, G. C., Verkhratsky, A., Yamanaka, K., Koistinaho, J., Latz, E., Halle, A., … Kummer, M. P. (2015). Neuroinflammation in Alzheimer's disease. *Lancet Neurology*, *14*(4), 388–405. https://doi.org/10.1016/S1474-4422(15)70016-5
Hescham, S., Liu, H., Jahanshahi, A., & Temel, Y. (2020). Deep brain stimulation and cognition: Translational aspects. *Neurobiology of Learning and Memory*, *174*, 107283. https://doi.org/10.1016/j.nlm.2020.107283
Hoover, W. B., & Vertes, R. P. (2012). Collateral projections from nucleus reuniens of thalamus to hippocampus and medial prefrontal cortex in the rat: A single and double retrograde fluorescent labling study. *Brain Structure and Function*, *217*, 191–209. https://doi.org/10.1007/s00429-011-0345-6
Iglesias, J. E., Augustinack, J. C., Nguyen, K., Player, C. M., Player, A., Wright, M., Roy, N., Frosch, M. P., McKee, A. C., Wald, L. L., Fischl., B., & van Leemput, K. (2015). A computational atlas of the hippocampal formation using ex vivo, ultra-high resolution MRI: Application to adaptive segmentation of in vivo MRI. *NeuroImage*, *115*, 117–137. https://doi.org/10.1016/j.neuroimage.2015.04.042
Iglesias, J. E., Insausti, R., Lerma-Usabiaga, G., Bocchetta, M., van Leemput, M., Greve, D., van der Kouwe, A., Caballero-Gaudes, C., & Paz-Alonso, P. (2018). A probabilistic atlas of the human thalamic nuclei combining ex vivo MRI and histology. *NeuroImage*, *183*, 314–326. https://doi.org/10.1016/j.neuroimage.2018.08.012
Jack, C. R., Petersen, R. C., Xu, Y. C., Waring, S. C., OBrien, P. C., Tangalos, E. G., Smith, G. E., Ivnik, R. J., & Kokmen, E. (1997). Medial temporal atrophy on MRI in normal aging and very mild Alzheimer's disease. *Neurology*, *49*(3), 786–794. https://doi.org/10.1212/WNL.49.3.786
Jayachandran, M., Linley, S., Schlecht, M., Mahler, S. V., Vertes, R. P., & Allen, T. A. (2019). Prefrontal Pathways Provide Top-Down Control of Memory for Sequences of Events. *Cell Reports*, *28*(3), 640–654. https://doi.org/10.1016/j.celrep.2019.06.053
Jenkinson, M., Beckmann, C. F., Behrens, T. E. J., Woolrich, M. W., & Smith, S. M. (2012). FSL. *NeuroImage*, *62*(2), Article 2. https://doi.org/10.1016/j.neuroimage.2011.09.015
Jeurissen, B., Tournier, J. D., Dhollander, T., Connelly, A., & Sijbers, J. (2014). Multi-tissue constrained spherical deconvolution for improved analysis of multi-shell diffusion MRI data. *NeuroImage*, *103*, 411–426. https://doi.org/10.1016/j.neuroimage.2014.07.061
Jones, D. K. (2008). Studying connections in the living human brain with diffusion MRI. *Cortex*, *44*(8), 936–952. https://doi.org/10.1016/j.cortex.2008.05.002
Kaye, J. A., DeCarli, C., & Luxenberg, J. S. (1992). The significance of age-related enlargement of the cerebral ventricles in healthy men and women measured by quantitative computed X-ray tomography. *J Am Geriatr Soc*, *40*(3), 225–231.
Kellner, E., Dhital, B., Kiselev, V. G., & Reisert, M. (2016). Gibbs-ringing artifact removal based on local subvoxel-shifts. *Magnetic Resonance in Medicine*, *76*, 1574–1581. https://doi.org/10.1002/mrm.26054
Lee, M. D., & Wagemakers, E.-J. (2015). *Bayesian Cognitive Modeling: A practical Course*. Cambridge University Press.
Li, K., Wang, S. Y., Luo, X., Zeng, Q. Z., Jiaerken, Y., & Xu, X. P. (2020). Progressive memory circuit impairments along with alzheimer's diseaseneuropathology spread: Evidence from in vivo neuroimaging. *Cerebral Cortex*, *30*, 5863–5873. https://doi.org/10.1093/cercor/bhaa162
Lin, K. A., Choudhury, K. R., Rathakrishnan, B. G., Marks, D. M., Petrella, J. R., & Doraiswamy, P. M. (2015). Marked gender differences in progression of mild cognitive impairment over 8 years. *Alzheimers Dement*, *1*(2), 103–110. https://doi.org/10.1016/j.trci.2015.07.001
Lo, C. Y., Wang, P. N., Chou, K. H., Wang, J., He, Y., & Lin, C. P. (2010). Diffusion tensor tractography reveals abnormal topological organization in structural cortical networks in Alzheimer's disease. *Journal of Neuroscience*, *30*, 16876–16885. https://doi.org/10.1523/JNEUROSCI.4136-10.2010
McElreath, R. (2020). *Statistical Rethinking* (2nd ed.). CRC Press.
Mitchell, A. J., & Shiri-Feshki, M. (2009). Rate of progression of mild cogni- tive impairment to dementia—Meta-analysis of 41 robust inception cohort studies. *Acta Psychiatr Scand*, *119*, 252–265. https://doi.org/10.1111/j.1600-0447.2008.01326.x
Mito, R., Raffelt, D., Dhollander, T., Vaughan, D. N., Tournier, J. D., Salvado, O., Brodtmann, A., Rowe, C. C., Vollemagne, V. L., & Connelly, A. (2018). Fibre-specific white matter reductions in Alzheimer's disease and mild cognitive impairment. *Brain*, *141*(3), 888–902. https://doi.org/10.1093/brain/awx355
Nasrabady, S. E., Rizvi, B., Goldman, J. E., & Brickman, A. M. (2018). White matter changes in Alzheimer's disease: A focus on myelin and oligodendrocytes. *Acta Neuropathologica*, *6*.
Papez, J. W. (1937). A proposed mechanism of emotion. *Archives of Neurology Psychiatry*, *38*(4), 725–743. https://doi.org/10.1001/archneurpsyc.1937.02260220069003
Parker, C. S., Veale, T., Bocchetta, M., Slattery, C. F., Malone, I. B., Thomas, D. L., Schott, J. M., Cash, D. M., & Zhang, H. (2021). Not all voxels are created equal: Reducing estimation bias in regional NODDI metrics using tissue-weighted means. *NeuroImage*, *245*. https://doi.org/10.1016/j.neuroimage.2021.118749

Pasternak, O., Sochen, N., Gur, Y., Intrator, N., & Assaf, Y. (2009). Free water elimination and mapping from diffusion MRI. *Magnetic Resonance in Medicine*, *62*(3), 717–730.

Patanaude, B., Smith, S. M., Kennedy, D. N., & Jenkinson, M. A. (2011). Bayesian model of shape and appearance for subcortical brain segmentation. *NeuroImage*, *56*, 907–922. https://doi.org/10.1016/j.neuroimage.2011.02.046

Petersen, R. (2007). Mild Cognitive Impairment: Current Research and Clinical Implications. *Seminars in Neurology*, *27*, 22–31. https://doi.org/10.1055/s-2006-956752

Petersen, R. C., Smith, G. E., Waring, W. C., Ivnik, R. J., Tangalos, E. G., & Kokmen, E. (1999). Mild cognitive impairment—Clinical characterization and outcome. *Archives of Neurology*, *56*, 303–308. https://doi.org/10.1001/archneur.56.3.303

Pierpaoli, C., & Basser, P. J. (1996). Toward a quantitative assessment of diffusion anisotropy. *Magnetic Resonance in Medicine*, *36*, 893–906. https://doi.org/10.1002/mrm.1910360612

Racin, A. M., Adluru, N., Alexander, A. L., Christian, B. T., Okonkwo, O. C., Oh, J., Cleary, C. A., Birdsill, A., Hillmer, A. T., Murali, D., Barnhart, T. E., Gallagher, C. L., Carlsson, C. M., Rowley, H. A., Dowling, N. M., Asthana, S., Sager, M. A., Bendlin, B. B., & Johnson, S. C. (2014). Associations between white matter microstructure and amyloid burden in preclinical Alzheimer's disease: A multimodal imaging investigation. *Neuroimage Clinical*, *4*, 604–614. https://doi.org/10.1016/j.nicl.2014.02.001

Raffelt, D., Dhollander, T., Tournier, J.-D., Tabbara, R., Smith, R. E., Pierre, E., & Connelly, A. (2017). *Bias Field Correction and Intensity Normalisation for Quantitative Analysis of Apparent Fibre Density*. *25*, 3541.

Rayboud, C. (2010). The corpus callosum, the other great forebrain commissures, and the septum pellucidum: Anatomy, development, and malformation. *Neuroradiology*, *52*, 447–477. https://doi.org/10.1007/s00234-010-0696-3

Segonne, F., Dale, A. M., Busa, E., Glessner, M., Salat, D., Hahn, H. K., & Fischl, B. (2004). A hybrid approach to the skull stripping problem in MRI. *NeuroImage*, *22*(3), 1060–1075. https://doi.org/10.1016/j.neuroimage.2004.03.032

Shaikh, I., Beaulieu, C., Gee, M., McCreary, C. R., Beaudin, A. E., Valdes-Cabrera, D., Smith, E. E., & Camicioli, R. (2022). Diffusion tensor tractography of the fornix in cerebral amyloid angiopathy, mild cognitive impairment and Alzheimer's disease. *Neuroimage Clinical*, *34*. https://doi.org/10.1016/j.nicl.2022.103002

Smith, R. E., Tourner, J.-D., Calamante, F., & Connelly, A. (2015). SIFT2: Enabling dense quantitative assessment of brain white matter connectivity using streamlines tractography. *NeuroImage*, *119*, 338–351. https://doi.org/10.1016/j.neuroimage.2015.06.092

Smith, R. E., Tournier, J. D., Calamante, F., & Connelly, A. (2012). Anatomically-constrained tractography: Improved diffusion MRI streamlines tractography through effective use of anatomical information. *NeuroImage*, *62*, 1924–1938. https://doi.org/10.1016/j.neuroimage.2012.06.005

Smith, R. E., Tournier, J.-D., Calamante, F., & Connelly, A. (2015). The effects of SIFT on the reproducibility and biological accuracy of the structural connectome. *NeuroImage*, *104*, 253–265. https://doi.org/10.1016/j.neuroimage.2014.10.004

Smith, S. M. (2002). Fast robust automated brain extraction. *Human Brain Mapping*, *17*, 143–155. https://doi.org/10.1002/hbm.10062

Smith, S. M., Jenkinson, M., Woolrich, M. W., Beckmann, C. F., Behrens, T. E. J., Johansen-Berg, H., Bannister, P. R., De Luca, M., Drobnjak, I., Flitney, D. E., Niazy, R. K., Saunders, J., Vickers, J., Zhang, Y., De Stefano, N., Brady, J. M., & Matthews, P. M. (2004a). Advances in functional and structural MR image analysis and implementation as FSL. *NeuroImage*, *23*(Suppl 1), Article Suppl 1. https://doi.org/10.1016/j.neuroimage.2004.07.051

Smith, S. M., Jenkinson, M., Woolrich, M. W., Beckmann, C. F., Behrens, T. E. J., Johansen-Berg, H., Bannister, P. R., De Luca, M., Drobnjak, I., Flitney, D. E., Niazy, R. K., Saunders, J., Vickers, J., Zhang, Y., De Stefano, N., Brady, J. M., & Matthews, P. M. (2004b). Advances in functional and structural MR image analysis and implementation as FSL. *NeuroImage*, *23*(Suppl 1), S208-219. https://doi.org/10.1016/j.neuroimage.2004.07.051

Spires-Jones, T. L., & Hyman, B. T. (2014). The Intersection of Amyloid Beta and Tau at Synapses in Alzheimer's Disease. *Neuron*, *82*(4), 756–771. https://doi.org/10.1016/j.neuron.2014.05.004

Torrealba, E., Aguilar-Zerpa, N., Garcia-Morales, P., & Diaz, M. (2023). Compensatory mechanisms in Early Alzheiemr's Disease and Clinical Setting: The Need for Novel Neuropsychological Strategies. *J Alzheimers Dis Rep*, *7*(1), 513–525. https://doi.org/10.3233/ADR-220116

Tournier, J. D., Calamante, F., & Connelly, A. (2007). Robust determination of the fibre orientation distribution in diffusion MRI: Non-negativity constrained super-resolved spherical deconvolution. *NeuroImage*, *35*, 1459–1472. https://doi.org/10.1016/j.neuroimage.2007.02.016

Tournier, J. D., Calamante, F., & Connelly, A. (2010). Improved probabilistic streamlines tractography by 2nd order integration over fibre orientation distributions. *Proceedings of the International Society for Magnetic Resonance in Medicine*, *1670*.

Tournier, J. D., Calamante, F., Gadian, D. G., & Connelly, A. (2004). Direct estimation of the fiber orientation density function from diffusion-weighted MRI data using spherical deconvolution. *NeuroImage*, *23*, 1176–1185. https://doi.org/10.1016/j.neuroimage.2004.07.037

Tournier, J. D., Smith, R. E., Raffelt, D., Tabbara, R., Dhollander, T., Pietsch, M., Christiaens, D., Jeurissen, B., Yeh, C. H., & Connelly, A. (2019). MRtrix3: A fast, flexible and open software framework for medical image processing and visualisation. *NeuroImage*, *202*, 116–137. https://doi.org/10.1016/j.neuroimage.2019.116137

Tustison, N. J., Avants, B. B., Cook, P. A., Zheng, Y., Egan, A., Yushkevich, P. A., & Gee, J. C. (2010). N4ITK: improved N3 bias correction. *IEEE Transactions on Medical Imaging*, *29*, 1310–1320. https://doi.org/10.1109/TMI.2010.2046908

Tustison, N. J., Cook, P. A., Holbrook, A. J., Johnson, H. J., Muschelli, J., Devenyi, G. A., Duda, J. T., Das, S. R., Cullen, N. C., Gillen, D. L., Yassa, M. A., Stone, J. R., Gee, J. C., & Avants, B. B. (2021). The ANTsX ecosystem for quantitative biological and medical imaging. *Scientific Reports*, *11*(1), Article 1. https://doi.org/10.1038/s41598-021-87564-6

van Doorn, J., van den Bergh, D., Bohm, U., Dablander, F., Derks, K., Draws, T., Etz, A., Evans, N. J., Gronau, Q. F., Haaf, J. M., Hinne, M., Kucharsky, S., Ly, A., Marsman, M., Matzke, D., Gupta, A. R. K. N., Sarafoglou, A., Stefan, A., Voelkel, J. G., & Wagenmakers, E.-J. (2021). The JASP guidelines for conducting and reporting a Bayesian analysis. *Psychonomic Bulletin & Review*, *28*, 813–826. https://doi.org/10.3758/ s13423-020-01798-5.

Vann, S. D., Denby, C., Love, S., Montaldi, D., Renowden, S., & Coakham, H. B. (2008). Memory loss resulting from fornix and septal damage: Impaired supra-span recall but preserved recognition over a 24-hour delay. *Neurosychology*, *22*, 658–668. https://doi.org/10.1037/a0012542

Varela, C., Kumar, S., Yang, J. Y., & Wilson, M. A. (2014). Anatomical substrates for direct interactions between hippocampus, medial prefrontal cortex, and the thalamic nucleus reuniens. *Brain Structure and Function*, *219*, 911–929. https://doi.org/10.1007/s00429-013-0543-5

Veraart, J., Fieremans, E., & Novikov, D. S. (2016). Diffusion MRI noise mapping using random matrix theory. *Magnetic Resonance in Medicine*, *76*, 1582–1593. https://doi.org/10.1002/mrm.26059

Vertes, R. P., Hoover, W. B., Szgeti-Buck, K., & Leranth, C. (2007). *Nucleus reuniens of the midline thalamus: Link between the medial prefrontal cortex and the hippocampus*. *71*(4), 601–609. https://doi.org/10.1016/j.brainresbull.2006.12.002

Vertes, R. P., Linley, S., & Viena, T. (2022). Nucleus Reuniens: Circuitry, Function, and Dysfunction. In *Electrophysiological Recording Techniques* (101st ed., Vol. 55, pp. 55–101).

Villain, N., Desgranges, B., Viader, F. de la, Sayette, V., Mezenge, F., & Landeau, B. (2008). Relationships between Hippocampal Atrophy, White Matter Disruption, and Gray Matter Hypometabolism in Alzheimer's Disease. *Journal of Neuroscience*, *28*, 6174–6181. https://doi.org/10.1523/JNEUROSCI.1392-08

Wang, J., Zou, X.-N., Dai, Z., Xia, M., Zhao, Z., Zhao, X., J, J., Han, Y., & He, Y. (2012). Disrupted Functional Brain Connectome in Individuals at Risk for Alzheimer's Disease. *Biological Psychiatry*, *73*. https://doi.org/10.1016/j.biopsych.2012.03.026

Wang, S. S., Zhang, Z., Zhu, T. B., Chu, S. F., He, W. B., & Chen, N. H. (2018). Myelin injury in the central nervous system and Alzheimer's disease. *Brain Res Bull*, *140*, 162–168. https://doi.org/10.1016/j.brainresbull. 2018.05.003

Wen, Q., Risacher, S. L., Xie, L., Li, J., Harezlak, J., Farlow, M. R., Unverzagt, F. W., Gao, S., Apostolova, L. G., Saykin, A. J., & Wu, Y. C. (2021). Tau related white-matter alterations along spatially selective path ways. *NeuroImage*, *226*. https://doi.org/10.1016/j. neuroimage.2020.117560

Wolf, D., Fischer, F. U., Scheurich, A., & Fellgiebel, A. (2015). Non-Linear Association between Cerebral Amyloid Deposition and White Matter Microstructure in Cognitively Healthy Older Adults. *Journal of Alzheimers Disease*, *47*(1), 117–127. https://doi.org/10.3233/JAD-150049

Xu, W., & Sudhof, T. C. (2013). A Neural Circuit for Memory Specificity and Generalization. *Science*, *339*(6125), 1290–1295. https://doi.org/10.1126/science.1229534

Zhang, F., Daducci, A., He, Y., Schiavi, S., Seguin, C., Smith, R., Yeh, C. H., Zhao, T., & O'Donnell, L. J. (2021). Quantitative mapping of the brain's structural connectivity using diffusion MRItractography: A review. *arXiv.* https://doi.org/10.48550/arXiv.2104.11644

Zhang, H., Schneider, T., Wheeler-Kingshott, C. A., & Alexander, D. C. (2012). NODDI: practical in vivo neurite orientation dispersion and density imaging of the human brain. *NeuroImage*, *61*, 1000–1016. https://doi.org/10.1016/j.neuroimage.2012.03.072

Zhang, Y., Brady, M., & Smith, S. (2001). Segmentation of brain MR images through a hidden Markov random field model and the expectation-maximization algorithm. *IEEE Transactions on Medical Imaging*, *20*, 45–57. https://doi.org/10.1109/42.906424

Zhao, H., Cheng, J., Liu, T., Jiang, J., Koch, F., Sachdev, P. S., Basser, P. J., & Wen, W. (2021). Orientational changes of white matter fibers in Alzheimer's disease and amnestic mild cognitive impairment. *Human Brain Mapping*, *42*(16), 5397–5408. https://doi.org/10.1002/hbm.25628

Zhong, S., Lou, J., Ma, K., Shu, Z., Chen, L., Li, C., Ye, Q., Zhou, L., Shen, Y., Ye, X., & Zhang, J. (2023). Disentangling in-vivo microstructural changes of white and gray matter in mild cognitive impairment and Alzheimer's disease: A systematic review and meta-analysis. *Brain Imaging and Behavior, 17*, 764–777. https://doi.org/10.1007/s11682-023-00805-2